Dalton Transactions

ROYAL SOCIETY OF CHEMISTRY

PAPER

View Article Online
View Journal | View Issue

Cite this: *Dalton Trans.*, 2024, **53**, 17244

Mixed-ligand based water-stable Mn(II)-MOF for quick, sensitive, and reusable IFE-PET-RET facilitated detection of formaldehyde and Cr(VI)-oxoanions in real-field samples like food and industrial water: experimental and theoretical insights†

Udayan Mondal, [a,b] Somrita Nag,‡[a,b] Rajeshwari Pal ‡[a,b] and Priyabrata Banerjee *[a,b]

Received 24th September 2024,
Accepted 30th September 2024

DOI: 10.1039/d4dt02707h

rsc.li/dalton

We report the luminescence-based detection of Group-1 carcinogen formaldehyde (FA) and Cr(VI)-oxoanions with a mesoporous Mn(II)-MOF (**1**), featuring a uninodal 4-c net topology and linear 1D square channels forming a polymeric 2D network. The Mn-MOF *i.e.*, $[Mn(phen)(hia)(H_2O)]_\infty$ was solvothermally constructed using π-conjugated, chelating phenanthroline (phen) and μ^3–η^2:η^1 binding 5-hydroxyisophthalic acid (hia) ligands. The 2D rod-like crystallites of **1** demonstrated excellent phase purity, high thermal and photostability, and robustness under harsh conditions. The SCXRD and XPS studies established the structural framework and elemental composition, while the Hirshfeld surface analysis and NCI-RDG plot confirmed the presence of π–π stacking and weak interactions in **1**. We explored the bright-blue emission of **1** for recyclable and fast-responsive (~70 s) 'turn-off' detection of FA, with a low limit of detection (LOD) of 8.49 μM. Based on this, a 04-input-03-output molecular logic gate was proposed, which can be useful as a molecular switch for future applications. Furthermore, a unique experimental setup using the MOF film demonstrated ~57% quenching upon exposure to FA vapor (an indoor VOC). Additionally, **1** exemplified itself as an efficient probe towards Cr(VI)-oxyanions, depicting LODs of 79 and 170 ppb, Stern–Volmer constants (K_{SV}) of 16.13×10^4 and 12.73×10^4 M^{-1}, and response times of ~48 and ~40 s for CrO_4^{2-} and $Cr_2O_7^{2-}$, respectively. DFT calculations and specific wet-chemical investigations elucidated the FA detection to be triggered by photo-induced electron transfer (PET), while the Cr(VI)-sensing involved a combination of PET, the inner-filter effect (IFE), resonance energy transfer (RET), and electrostatic H-bonding interactions. The FA detection was validated using food samples (fish and meat) and wastewater specimens, achieving excellent recovery rates of ~92–95%. Furthermore, the MOF's efficacy in recognizing the Cr(VI)-species in complex matrices (coal mine wastewater, sewage, and tap water) was investigated to yield high K_{SV} values ($3.10–5.17 \times 10^4$ and $2.16–7.03 \times 10^4$ M^{-1} for CrO_4^{2-} and $Cr_2O_7^{2-}$), which demonstrated the probe's consistency and reliability.

Introduction

Rapid urbanization in the 21st century is often closely associated with increased industrial activity, leading to a greater demand for more chemical production. While economic growth has brought prosperity, the unrestricted expansion of industrialization has resulted in adverse environmental impacts, such as the release of toxic chemicals.[1–3] In this context, the presence of formaldehyde (FA) in water and food, even at a trace level, can pose risks to human health.[4] In general, FA plays a vital role in several biochemical processes, such as methylation and demethylation of DNA and RNA,

[a]*Electric Mobility and Tribology Research Group, CSIR-Central Mechanical Engineering Research Institute, M. G. Avenue, Durgapur 713209, West Bengal, India. E-mail: pr_banerjee@cmeri.res.in; https://www.cmeri.res.in https://www.priyabratabanerjee.in*

[b]*Academy of Scientific and Innovative Research (AcSIR), Ghaziabad 201002, Uttar Pradesh, India*

†Electronic supplementary information (ESI) available. CCDC 2337818. For ESI and crystallographic data in CIF or other electronic format see DOI: https://doi.org/10.1039/d4dt02707h

‡These authors contributed equally to this work.

memory formation, stimulation and suppression of brain function, genetic activities, *etc.*[5–8] However, FA, the simplest aldehyde among the reactive carbonyl species (RCS),[9] when present in abnormal concentrations, becomes a Group-1 carcinogen (IARC, 2004).[10,11] Immediate contact with liquid or vapor FA can irritate mucous membranes, the eyes, the nose, the throat, and skin,[4,12–14] while prolonged exposure to FA has been linked to respiratory issues, memory loss, neurological & autonomic disorders, pulmonary edema, myeloid leukaemia, *etc.*[11,15,16] Excessive usage of FA as a potent preservative and in other household purposes (*viz.* cosmetic items, adhesives, paints, home textiles, antiseptics, and so forth) ultimately results in its emission into the indoor atmosphere, as a volatile organic compound (VOC).[4] Other natural and anthropogenic actions, for instance, biomass combustion, degradation of humic substances, tobacco smoke, automobile exhaust, *etc.*, also stimulate the FA release in the environment.[17,18] Several regulatory agencies has set standards for acceptable FA levels. For instance, the WHO has imposed a standard limit of 80 ppb average FA concentration at 30 min exposure time,[15] whereas the OSHA[19] and ACGIH[20] have defined a permissible exposure limit (PEL) of 0.75 and 0.30 ppm for FA in an 8 hour work shift. The NIOSH, US considers 20 ppm of FA concentration to be 'immediately dangerous to life and health (IDLH)', while the irritation to the eyes, nose, and throat starts at levels as low as ~0.3 ppm in air.[19] Therefore, given its potential health risks, intuitive monitoring of FA in water and food has become an essential aspect of public health and environmental protection efforts.

On the other hand, high concentrations of heavy metal ions (HMs), anions, and various organic pollutants in industrial effluents have undoubtedly become another major issue.[3,21–25] Specifically, the Cr(VI)-oxoanions (*i.e.*, chromate and dichromate) are of great concern due to their severe toxicity, non-biodegradability, and unhindered bioaccumulation pathway through water intake.[26,27] CrO_4^{2-} and $Cr_2O_7^{2-}$ are extensively used in several industries such as glass manufacturing, agro-sectors, production of stainless steel, chromite manufacturing, oxidative dyeing, wood preservation, leather tanning, metallurgy, paint, *etc.*[28,29] Compared to other HMs, Cr^{6+}-oxyanions are exceedingly soluble in water over nearly the whole pH range, which worsens the contamination scenario.[30] The Cr(VI)-oxyanions are potent oxidizing agents and can contribute to several ailments in the human body, *viz.* visceral damage,[31] injuries to DNA,[32] disruption of the protein and enzyme system,[32] ulcers,[33] renal failure,[33] lung cancer,[33] gene mutation,[34] *etc.* The US EPA has enlisted hexavalent chromium as a 'priority pollutant' and hence restricted its threshold limit to <100 ppb,[26,35] whereas IARC has classified it as a first-class carcinogen.[28] Additionally, the WHO has set a standard limit of 50 μg L^{-1} for total chromium in drinking water.[36] Consequently, trace-level aqueous phase Cr(VI)-sensing has become an inevitable issue to be addressed.

To date, various sophisticated techniques such as gas and ion chromatography, spectrophotometry, high-performance liquid chromatography (HPLC), polarography, colorimetry, *etc.* have been employed for the quantitative detection of FA.[4,9,11,16] Similarly, several traditional procedures such as ion chromatography, atomic absorption spectrometry (AAS), inductively coupled plasma mass spectrometry (ICP-MS), X-ray dispersion, voltammetry, ion mobility spectroscopy (IMS), *etc.* have been explored to analyse the chromium content in water.[37–39] Yet, the methods require a trained operator, along with costly instrumentation, high power consumption, complicated sample preparation, time-consuming procedures, and less convenience for on-site analysis, along with selectivity issues, *etc.*, which limit their practical applications.[4,9,11,16] In this context, luminescent materials have been at the forefront of functional material-based toxic analyte sensing research due to their perceptibility to bare eyes, on-site technical simplicity, specificity, rapid response, *etc.*[16] For FA sensing, various luminescent probes, for example discrete organic molecules, organic–inorganic nanohybrids, nanoparticles, carbon dots, *etc.* have been explored.[9,11,40,41] Similarly, quantum dots, coordination polymers, molybdates, cationic organic frameworks, nanocomposites, *etc.*, have been utilized for luminescence-based Cr(VI)-oxoanion detection.[28,34,42–45] However, there still exists room for further improvement, considering a few loopholes such as delayed response, detection in organic/organo-aqueous medium, low sensitivity, poor selectivity, no exploration towards real-life samples, *etc.* Under these circumstances, crystalline porous materials (CPMs), particularly luminescent metal–organic frameworks (LMOFs), are reliable candidates for discerning the detection of a broad category of organic and inorganic pollutants.[46] LMOFs have been registered as competent sensing materials towards organic small molecules, cations, gases, pH, biomarkers, *etc.* in recent years owing to many promising features, such as high color purity, a wide lifetime range, sharp emission, high quantum yield, *etc.*[4]

Based on these facts, we herein report an Mn(II)-MOF $[Mn(phen)(hia)(H_2O)]_\infty$ using a π-conjugated 1,10-phenanthroline (phen) linker and a bridging 5-hydroxy isophthalic acid (hia) co-ligand for recyclable, selective and sensitive luminescence quenching-based identification of carcinogenic FA and lethal Cr(VI)-species in low detection threshold. Our choice of MOF linkers is based on the following facts: (a) firstly, the N-donor, chelating phen ligand is planar, rigid, redox-stable, heteroaromatic and highly emissive (with close-lying π–π* and n–π* singlet excited states), which has been broadly explored in coordination chemistry,[47] and (b) isophthalate and its derivatives (*viz.* V-shaped 5-nitro/sulfo/hydro/amino-isophthalates, *etc.*) have attracted much interest lately, due to their active participation in creating intriguing architectures with new topologies and helical chains.[48] Notably, Lewis acidic Mn-based functional frameworks have been explored for several luminescence-based applications, for example sensing of explosives,[49] amino acids,[50] HMs,[51] aromatic amines,[52] *etc.* Here, the Mn-MOF (**1**) was thoroughly characterized by several analytical tools (single crystal and powder XRD, TGA, FESEM, EDX, XPS, FT-IR, *etc.*), that exhibited phase purity, thermal stability, robustness under harsh conditions, permanent mesoporosity with an irregular rod-like surface morphology and homogeneous atomic distribution. The MOF exemplified

itself as an efficient and rapid aqueous-phase sensory platform towards FA, CrO_4^{2-} and $Cr_2O_7^{2-}$ with limit of detection (LOD) values of 8.49, 0.41 and 0.59 μM, respectively. Furthermore, based on the distinct response of the interacting analyte (FA), logical functions (molecular-level arithmetic computations based on the Boolean logic) were performed and subsequently a unique molecular logic circuitry was proposed for FA sensing. In addition, vapor-phase FA detection was accomplished. The co-existence of RET, PET, IFE, electrostatic weak interactions (H-bonding), collisional quenching, *etc.* was accounted for the exceptional sensing performance towards FA and Cr(VI)-oxoanions. One step ahead, the quantification of targeted analytes from various complex matrices (fish and meat samples, sewage and wastewater specimens, *etc.*) was accomplished, with excellent recovery rates (~92–95% for FA, ~90–101% for CrO_4^{2-}, and ~82–101% for $Cr_2O_7^{2-}$). The presented outcomes are unique in their category and will certainly appeal to a broader scientific audience toward further MOF-sensor-based research.

Experimental section

Synthesis protocol of $[Mn(phen)(hia)_3]_\infty$ (1)

A mixture of the organic linkers *i.e.*, π-conjugated N-donor phen (13.52 mg; 0.075 mmol) and bridging dicarboxylate hia (26.40 mg; 0.125 mmol) was first dissolved in 4 ml of dimethyl formamide (DMF). Under the influence of high temperature (120 °C), DMF is hydrolyzed to produce a mild base dimethylamine, which facilities the deprotonation of the hia ligand. To this, an aqueous solution (2 ml) of [$(CH_3COO)_2Mn{\cdot}4H_2O$ (15.44 mg; 0.063 mmol)] was added and the mixture was sonicated for ~10 minutes to obtain a clear solution. The mixture was taken in a 15 mL oven-dried glass vial, tightly capped and transferred to a preheated oven (Scheme 1). After ~36 h, light green colored crystals were obtained (yield: ~83%), washed with a 2 : 1 mixture of DMF–H_2O and subsequently collected by filtration. Solid state elemental analysis for dried $C_{20}H_{12}MnN_2O_5$, H_2O: calculated C, 55.44%; H, 3.26%; N, 6.47%; found C, 54.25%; H, 3.02%; N, 5.52%.

Fluorescence sensing of aldehydes and oxoanions

First, 1 mg of compound **1** was finely ground using a mortar and suspended in 5 mL of acetonitrile (ACN) to prepare the sensor suspension. The MOF emulsion was then subjected to ultrasonic treatment for approximately 15 minutes to ensure further homogenization. Next, 2 mL of the stabilized suspension was transferred to a 5 mL quartz cuvette, and the photoluminescence (PL) response was recorded in triplicate at room temperature under an inert atmosphere. The analyte solutions (concentration: 1 mM for aldehyde and common organosolvents; 10^{-4} M for oxyanions) were prepared in Milli-Q water (MW). The PL response of the control and each step of incremental addition of analytes to it was recorded in an instantaneous manner. The quenching efficiency (QE, in %) was deduced as: QE (%) = $(1 - I/I_0) \times 100$, where I_0: initial PL intensity, I: quenched PL intensity after each addition (of the analyte).

Vapor-phase FA sensing

Instigated by the solid-state emissive nature of **1** and high vapor pressure of FA, the present study was extended towards

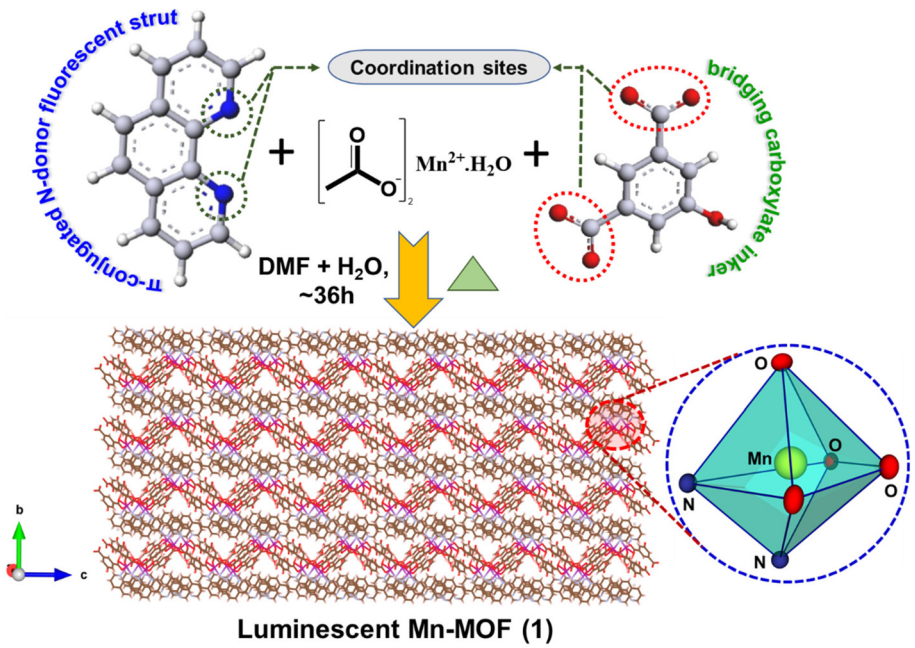

Scheme 1 Synthesis protocol for the luminescent Mn-MOF (**1**).

FA vapor detection. For this, a MOF suspension was drop-cast on a finely cut quartz glass substrate of suitable size. The extra solvent was evaporated and the glass-substrate was placed inside a 5 mL sealed cuvette. Next, ~300 μL of FA was placed at the bottom of the cuvette and it was completely sealed (Fig. S33, ESI†). Consequently, time-dependent (0–30 min) PL response was documented, keeping the glass-substrate in a front-facing alignment.

Fluorescence recyclability study

The regenerative PL response of **1** towards FA, CrO_4^{2-} and $Cr_2O_7^{2-}$ sensing was examined. After completion of the first sensing event, the MOF-analyte emulsion was centrifuged at 3000 rpm (~15 min), filtered and washed with adequate Milli-Q water. The collected powder sample was oven-dried and was employed for the next cycle of PL sensing experiment.

Results and discussion

Crystal structure, Hirshfeld surface and NCI-RDG analysis of 1

Single crystal XRD analysis showed that **1** ($C_{20}H_{12}MnN_2O_5$, H_2O) crystalizes in a monoclinic system with space group $P2/n$ (No. 13) with $Z = 4$ (see Table S1, ESI and experimental section, ESI† for data collection and refinement details). The asymmetric unit of **1** holds one Mn(II) centre coordinated with one π-conjugated, rigid phen ligand in a bidentate chelating fashion and with the $-COO^-$ moiety of the hia^{2-} co-ligand in *O*-monodentate mode (see the ORTEP of **1**, Fig. S1, ESI†). The asymmetric unit further contains one water of crystallization, participating in H-bonding with carboxylate ends of the hia^{2-} co-ligand. The entrapped H_2O molecules within the framework are shown in Fig. 1d. A close inspection depicts that the hexa-coordinated Mn(II) centre is surrounded by four oxygen atoms

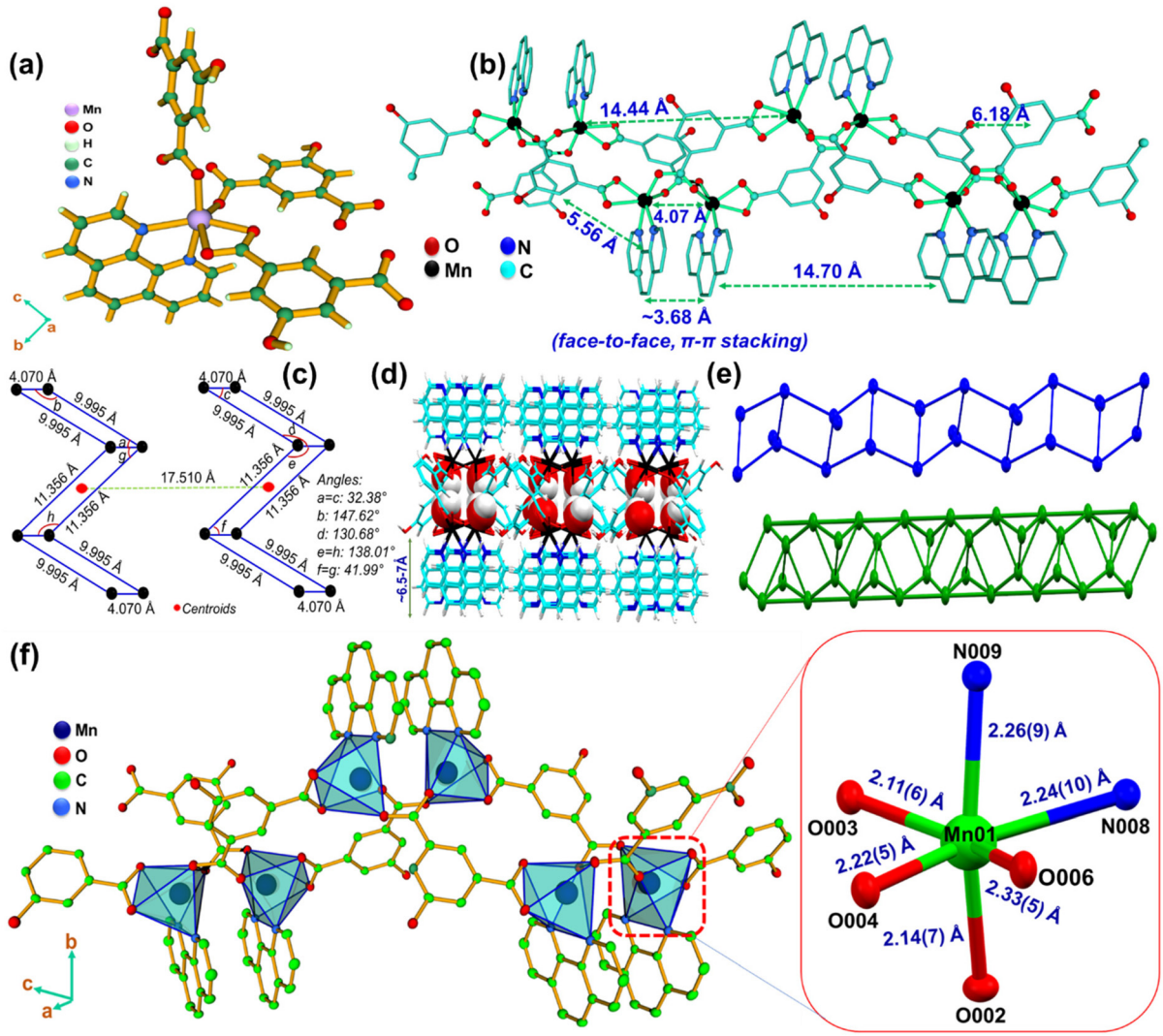

Fig. 1 (a) Complete coordination environment of the Mn(II) center in **1**; (b) depiction of the interatomic distance of Mn-centers, phen linkers and observation of face-to-face π–π stacking in **1**; (c) repetition of the linear 1D square channel formed by the metal nodes in **1**; (d) entrapped H_2O moieties within the framework in **1**; (e) 4-c uninodal net topology of **1** in standard (blue) and edge net (green) simplification methods; and (f) formation of the 2D-Network in **1**, along with the representation of distorted *Oh* geometry of the metal center.

(O3, O4, O2, O6) from three distinct hia^{2-} (5-hydroxyisophthalate) anions, and two nitrogen atoms (N8 and N9) from the chelating phen ligand in a distorted octahedral environment, showing Mn1–N8 and Mn1–N9 bond angles of 2.24(10) and 2.26(9) Å, respectively, along with Mn–O distances in the range from 2.11(6) to 2.33(5) Å (Fig. 1a, f and Table S2, ESI†). The *trans* angles around the Mn1 centre were observed to be 144.03 (6)° (O4–Mn1–O8), 147.15(6)° (O6–Mn1–O3), and 164.74(7)° (O2–Mn1–N9), whereas the equatorial angles were detected in the range of 57.84(6)° to 120.38(6)°, conferring high amount of distortion in its *Oh* arrangement (Table S3, ESI†). Here, one hia^{2-} coordinates with three Mn(II)-centers in an overall μ^3–η^2:η^1 bonding mode. Specifically, among the three hia^{2-} ligands around one Mn(II)-centre, one hia^{2-} binds in a bidentate chelating fashion, while the other two hia^{2-} binds in bidentate bridging mode, which ultimately facilitates the polymeric growth in **1** (Fig. 1a, b and Fig. S2–S5, ESI†). The interatomic distances between the Mn-centers and the occurrence of face-to-face π–π stacking between the adjacent phen linkers in **1** are shown in Fig. 1b and Fig. S5, ESI.† The metal nodes in **1**, along with its ligation environment, cumulatively create the linear 1D square channels, the repetition of which promotes the formation of the polymeric 2D network, as observed in Fig. 1c and Fig. S6, ESI.† From the topological point of view, **1** exhibited a 4-c net uninodal topology with Schläfli symbol {3^3.4^2.5} (Fig. 1e).

Furthermore, the existence of intermolecular interactions in **1** was substantiated by Hirshfeld surface analysis and 2D fingerprint plots, using CrystalExplore 3.1.[53,54] The Hirshfeld surface analysis was mapped over d_{norm} in the range of −0.1 to 1.5 Å, curvedness from −4.0 to 0.4 Å and shape index from −1.0 to 1.0 Å, where the normalized contact distance (d_{norm}) can be denoted as $d_{norm} = \{(d_i - r_i^{vdW})/r_i^{vdW}\} + \{(d_e - r_e^{vdW})/r_e^{vdW}\}$ (where d_e and d_i are distances from a given point on the surface to the nearest atom, outside and inside respectively; r^{vdW} is the van der Waals radius for a particular atom situated on the surface).[55] In the d_{norm} figure with blue–red–white colour conventions, the red colour denotes greater interaction, blue colour indicates longer contacts and white signifies contacts at van der Waals separation (Fig. S7, ESI†). The resulting 2D fingerprint plot derived from the Hirshfeld surface analysis provided a summary of the combination of d_e and d_i across the surface of the MOF (**1**). The curvedness surface depicted flat regions indicating the low curvedness around the phen aromaticity, whereas the red and blue triangles were observed in the shape index surface, which cumulatively indicated the occurrence of π–π interactions in **1** (Fig. S7b and c, ESI†). The weak interactions present in **1** were comprehensively identified using non-covalent interaction (NCI) analysis, aided by reduced density gradient (RDG) calculations.[56,57] The RDG is a mathematical quantity resulting from the electron density of a molecule, which can be visualized as an isosurface around the atoms, highlighting regions where the electron density is either accumulated or depleted. Here, the green, blue and red isosurfaces indicate attractive van der Waals interactions, H-bonding and steric repulsion between atoms, respectively.[56,57] For this purpose, the electron density (ρ) and RDG were used following the equation: $RDG = \left[\frac{1}{2(3\pi)^{1/3}} \frac{\nabla\rho}{\rho^{3/4}}\right]$.[58] Fig. S8, ESI† shows NCI descriptor plots for **1** from their electron density (ρ) distributions, illustrating the presence of attractive forces (H-bonding, van der Waals) along with steric repulsive interactions within the asymmetric unit of **1**, color-coded in blue, green and red respectively, with RDG set at 0.5 at. units and sign (λ_2) × ρ isovalue in the range of −0.035 to 0.020 at. units.

Structural characterization of 1

The PXRD pattern of the dried and ground crystals of bulk-phase synthesized **1** was recorded (2θ range: 5–50°), which superimposed exactly with the simulated pattern (Fig. 2a), representing its phase purity and thorough regularity in both bulk and microscale.[49,50,59,60] The observed sharp and narrow peaks further validated the high degree of crystallinity in **1**, where 2θ peaks at ∼10°, ∼15°, ∼19° and ∼25° arose probably due to the (110), (100), (200) and (310) planes.[61–63] To examine the chemical stability of **1**, we investigated its PXRD pattern when soaked in water (detection medium), mild acid (pH ∼5), and mild base (pH ∼10), and kept in open air for 7 days.[64] As evidenced in Fig. S9, ESI,† an almost intact PXRD pattern was recorded in all cases, affirming the high robustness of **1** against harsh chemical conditions. The TGA profile of **1** sheds light on its thermal stability (Fig. S10, ESI†). The first weight loss (∼3.57%) in the 80–115 °C range was observed possibly due to detachment of the entrapped water molecules. Next, we observed unwavering stability of **1** up to ∼370 °C, after which ∼4.5% weight loss occurred up to ∼460 °C, indicating the start of structure disruption. Accordingly, a steep slope afterward was realized up to ∼550 °C with rapid weight loss (∼33.4%), confirming the collapse of the ligand backbones and the polymeric network at this juncture. The microstructure of **1** was recorded from FE-SEM images. The surface of **1** exhibited polycrystalline nature, consisting of irregular and aggregated 2D rod-like crystallites along with grains of undefined morphology (Fig. 2b and Fig. S11, ESI†).[65] The elemental X-ray mapping image and EDAX spectra of **1** have been provided in Fig. S12 and S13, ESI,† asserting steady distribution of each constituting element (Mn, O, C, N) in **1**.

The surface atomic composition of **1** was validated through the XPS study (Fig. 2c–g). The survey scan of **1** displayed four firm peaks at binding energies of 284.40 (C 1s),[66] 399.51 (N 1s),[67,68] 531.57 (O 1s),[67,69] 639.07 and 652.42 eV (Mn 2p),[70,71] with a weak peak at 47.72 eV (Mn 3p)[72] (see Fig. 2c). The deconvolution of the C 1s spectra shows three peaks at 284.43 (main component peak, for C═C), 285.45 (C–O/C–N), and 287.88 eV (C═O) in Fig. 2d.[66,67] The deconvoluted O 1s spectra exhibit three peaks, at 530.76, 531.90, and 533.136 eV, corresponding to Mn–O, C═O, and C–O/O–H bonds, respectively (Fig. 2e).[67,70,72] Furthermore, the deconvolution of the N 1s signal resulted in two peaks at 399.03 eV and 400.05 eV corresponding to Mn–N and C–N/C═N binding, respectively (Fig. 2f).[27,73] For Mn 2p

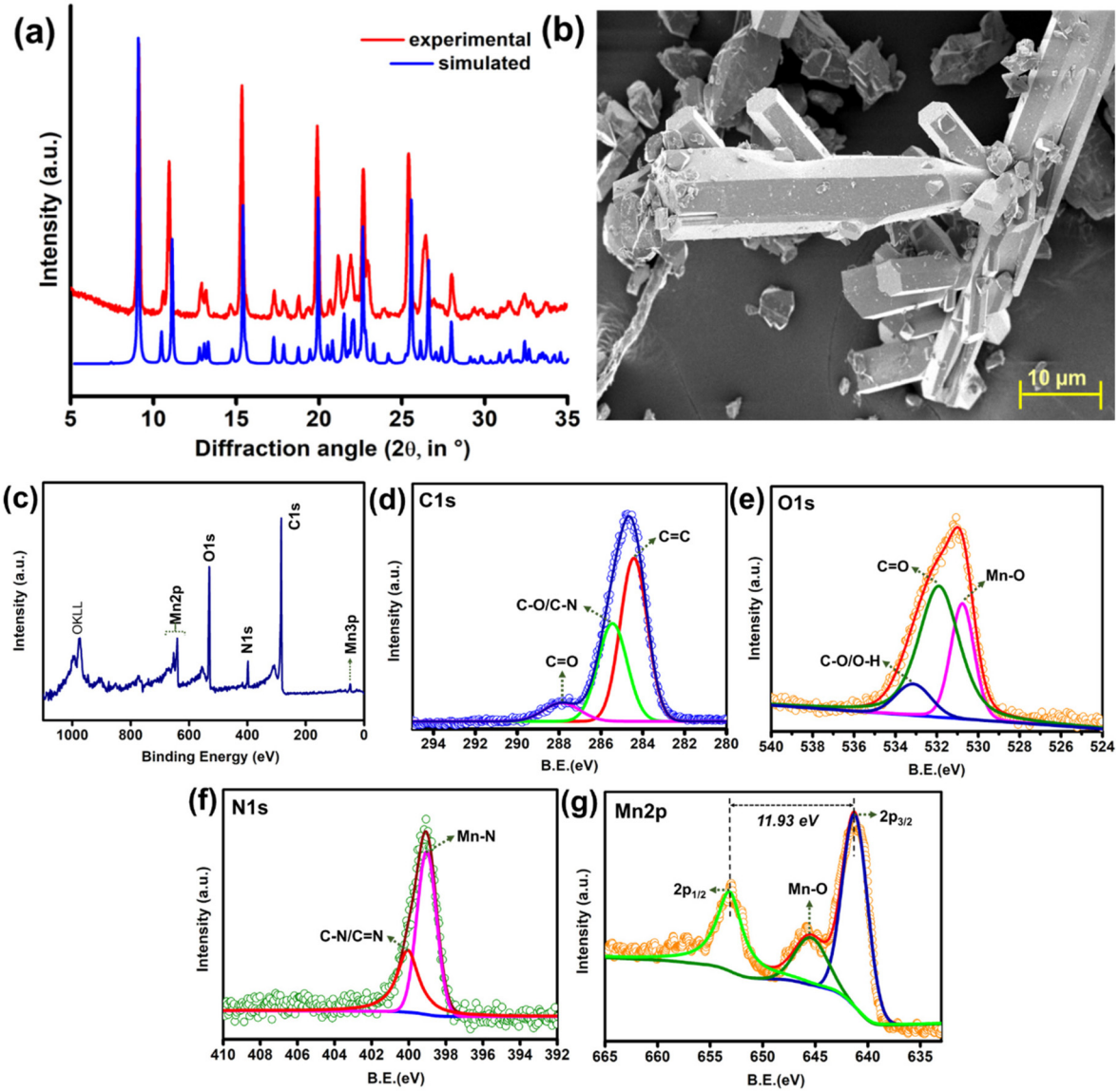

Fig. 2 (a) overlapping of powder XRD pattern of **1** (experimental and simulated); (b) FE-SEM morphology of **1**; (c–g) XPS spectra: survey scan and deconvoluted curves of C 1s, O 1s, N 1s and Mn 2p.

spectra, three deconvoluted peaks at binding energies of 641.21, 653.14, and 645.37 eV were also evidenced, indicating Mn $2p_{3/2}$ and Mn $2p_{1/2}$ orbitals, and Mn–O bonds (Fig. 2g).[70–72] The atomic composition was observed to be C 1s (71.06%), N 1s (6.87%), O 1s (19.88%), and Mn 2p (2.19%) from the XPS analysis. The surface area and pore size of **1** were calculated by conducting the N_2 absorption–desorption experiment (at 77 K).[74] From the gas sorption isotherm and linear fitting (R^2 = 0.99) of the BET equation at low relative pressure (Fig. S14a and b, ESI†), compound **1** exhibited a low surface area (18.39 $m^2\ g^{-1}$), which is comparable to several previously reported isophthalate-based MOFs.[75,76] Furthermore, the as-synthesized MOF revealed the average pore diameter ~3.63 nm (d$V(r)$ *vs.* pore radius plots, following the BJH method, Fig. S14c, ESI†). From the NLDFT studies, an average half pore width of ~1.45 nm (with peak pore volume at ~1.33–1.51 nm) was achieved, implying the presence of 'narrow mesopores' as well as small overall pore volume in **1** (Fig. S14d and Table S4, ESI†).[74,77]

The presence of π–π stacking was noticed in the spatial expansion of **1**, which likely restricted the adjacent 1D chains from coming closer than the van der Waals distance, finally creating interlayer voids.[50] Next, the functional groups and the Mn–O, Mn–N binding in **1** was confirmed by FT-IR spectroscopy (*vide* Fig. S15, ESI†). First, the sharp bands at 738 cm^{-1} and 857 cm^{-1} arose due to the out-of-plane C–H deformation (ν_{11} mode of phen pyridines) and the H atoms attached with the central ring, respectively.[27,78] While bonding with the metal centre, this sharp peak at 738 cm^{-1} displayed splitting, thus producing strong and weak signals

at 729 and 780 cm^{-1} respectively. This is expected, as the primary chelation effect is on the phen-N. Among the C–C and C–N stretching vibrations from 1400 to 1650 cm^{-1}, the strong band at 1421 cm^{-1} for the ν_{14} mode of the pyridine ring also broadens and splits on weak signals, owing to the readjustment of electron density in **1**. For hia, the peaks at 3357, 1700, and 1422 cm^{-1} appeared for O–H stretching, C═O stretching, and O–H bending vibrations. In coordination with the Mn(II)-centre, the peaks at 1700 cm^{-1} disappeared, while the peak at 1422 cm^{-1} diminished, affirming firm ligation with the metal centres. Following the unfolding of the structural aspects, **1** was finely ground and dispersed in acetonitrile medium to inspect its sensor applications. The AFM surface profile of the MOF–acetonitrile emulsion was recorded (Fig. S16, ESI†), exhibiting a well-dispersed state and an average surface roughness value of ~116.16 nm, enabling effective interface-driven interactions with the analytes.[3,23]

Photophysical characterization of 1

After the validation of the structural features, the photophysical characteristics were unveiled. The presence of N,O-like strong donor centers and high conjugation in **1** certainly plays a crucial part in guiding the photophysical behaviour. First, 1 mg of phen and hia were solvated in 5 ml acetonitrile (ACN). The ligand phen displayed a sharp absorption band at 240 nm (λ_{max}), while hia exhibited an intense band at 290 nm, owing to π–π* and/or n–π* electronic transitions within the framework.[75] The highest absorption peak (λ_{max}) of **1** (dispersed in acetonitrile, with a concentration of 1 mg mL^{-1}) was recorded at 270 nm (Fig. S17, ESI†). Therefore, the λ_{max} values of hia and phen shifted by 20 nm (hypsochromic) and 30 nm (bathochromic) when they ligated with the Mn^{2+} in **1**. This observation clearly proves the firm ligation of the metal node with organic linkers.[27,79] The ligands phen and hia displayed photoluminescence (PL) peaks (λ_{em}) at ~445 nm and ~340 nm, with moderate blue emission (see CIE coordinates in Fig. S18, ESI†). However, upon excitation at 270 nm, **1** showed brighter emission in the blue region (λ_{em}: 435 nm) with ~1.10 and ~1.26 fold enhanced intensity as compared to the struts (phen and hia respectively) (Fig. S18, ESI†). The higher luminescence of **1** possibly arose as a consequence of 'ligand-based emission' along with contributions from ligand-to-metal, intra-ligand (π–π* and n–π*), metal-to-ligand charge transfer pathways and considerable π–π weak interactions between the constituting aromatic linkers of **1**.[75,76,80–83] It is obvious that the Mn(II)-salt is non-emissive in acetnitrile. However, when it covalently coordinates with the struts, the polymeric architecture experiences a significant degree of conformational rigidity and enhanced intermolecular forces. As a result, the excited state becomes more populated and 'chelation enhancement fluorescence (CHEF)'[80] is observed. The Mn(II)-centre is paramagnetic in nature. Yet, relevant literature demonstrates that MOFs' high emission phenomenon is mostly centralized on the ligand backbone, which encouraged us to use **1** in sensory applications.[84–86] Furthermore, we explored the equation $\Phi_{MOF} = \Phi_{Ref} \times \frac{(A_{Ref} \times F_{MOF} \times \eta_{MOF}^2)}{(A_{MOF} \times F_{Ref} \times \eta_{Ref}^2)}$ (where *A*: absorption, *F*: integrated intensity (area) and η: refractive index) for calculation of the quantum yield (Φ). Here, Φ was evaluated to be 0.40 for **1** (taking phenanthrene as the reference standard). We also inspected the luminescence of **1** in different solvents (dispersed conditions) of varying polarity (dioxane, dimethylformamide (DMF), isopropanol, methanol, tetrahydrofuran, water, and acetonitrile). Among these, **1** exhibited the highest emission in DMF and acetonitrile media (Fig. S19, ESI†). However, we used the **1**-acetonitrile dispersion as the sensory probe, considering its more user-friendly nature. In all cases, the emission occurred in the blue region, as seen from the CIE coordinates in Fig. S19, ESI.† The emission profile of **1** was also recorded at different excitation wavelengths (260–285 nm), and in all instances, **1** displayed an emission band at ~435–440 nm. This confirmed the inherent emissive nature of **1**, with a true emission peak centred at ~435 nm (Fig. S20, ESI†). Furthermore, to affirm the stability of the dispersed MOF emulsion under constant photoirradiation, we recorded a time-dependent emission profile of **1** (Fig. S21, ESI†). Under incessant photoexcitation for 0–60 minutes, the PL intensity of **1** was only slightly quenched (8.33%). This negligible alteration of the PL profile confirmed the satisfactory homogenization of **1** and indicated no structural collapse under continuous exposure to the light source. Additionally, the MOF sensor didn't exhibit any significant quenching when water (~500 μL), a universal quencher, was added to the sensor dispersion (Fig. S22, ESI†).[87] Therefore, **1** could be successfully employed for toxic analyte recognition purposes from water medium. Furthermore, the Mn-MOF (**1**) depicted an emissive nature in the solid, powdered form. In the solid state, the emission profile of **1** exhibited a broad shoulder at 425 nm along with a sharp peak at 480 nm (Fig. S23, ESI†). The slight variance of the solid-state PL spectra from the solution state may be accredited to the close packing in solids, hence prompting a few additional weak interactions (H-bonding, van der Waals interaction, intermolecular force of attraction, *etc.*).[59,81]

Solution and vapour phase sensing of FA

The luminescent Mn-MOF (**1**) was next explored for selective detection of FA, which is the simplest aldehyde (RCS) and is frequently used as a solvent and preservative. We first prepared 1 mM aqueous solution of different aldehydes and common organosolvents, such as FA, benzaldehyde (BA), furfural (FuA), glutaraldehyde (GluA), glyoxal (OxA), propionaldehyde (PrA), valeraldehyde (VaA), syringaldehyde (SyA), acetone, chloroform, dioxane, methanol, ethanol and tetrahydrofuran (THF).[15] The chemical structures of the analyte series are provided in Fig. S24, ESI.† First, the interaction of the aqueous aldehydes with the MOF-sensor was inspected. In this context, direct addition of ~400 μL, 1 mM aldehyde solutions to ~400 μL sensor emulsion (host : guest = 1 : 1 v/v) depicted that under UV-irradiation, the emission profile of **1** drastically

quenched only for FA (Fig. S25, ESI†). Similarly, 400 μL, 1 mM solvents couldn't alter the luminescence of **1**. To quantify the sensing phenomenon, the inherent PL profile of **1** was monitored under the gradual addition of 1 mM of all the analytes (Fig. 3a, Fig. S26, ESI†). The order of the quenching phenomenon was recorded as follows: FA (75.82%) ≫ OxA (34.48%) > chloroform (29.71%) > BA (29.20%) > THF (28.48%) > Dxn (27.25%) > MeOH (26.11%) > EtOH (24.95%) > GluA (24.45%) > SyA (24.38%) > VaA (21.37%) > acetone (19.62%) > FuA (19.38%) > PrA (11.25%) (Fig. 3b). The highest quenching of ~76%, along with a slight blue shift of the emission band of **1**, confirmed its high selectivity towards FA. At this moment, we paid attention to further analysis of the emission profile of the **1**-FA adduct. The distinct change in CIE coordinates of **1** and **1**-FA adduct is given in Fig. S27, ESI.† Next, we introduced the Stern–Volmer plot[27,59] for FA titration, which is: $[I_0/I] - 1 = K_{SV} \times [A]$, ($K_{SV}$ is the quenching constant in M^{-1} unit, I_0 is the initial PL intensity of the sensor, I is the PL intensity of the **1**···FA adduct in each step of FA addition and [A] signifies the analyte concentration). Here, the S–V plot was observed to be non-linear in nature (Fig. 3c). The deviation from linearity may suggest the existence of long-range energy transfer or, the occurrence of static and/or dynamic quenching pathways or, self-absorption or, the inner-filter effect (IFE), *etc.*[59,75,79,88] A closer inspection depicts that the S–V plot follows linearity in the lower FA concentration range of 0.12–0.80 × 10^{-3} M (R^2: 0.98), but arcs upwards beyond this (Fig. S28, ESI† and Fig. 3c). From the linear range, the K_{SV} value was assessed to be 8.90 × 10^3 M^{-1}. Furthermore, the average fluorescence lifetime (τ_{avg}) was calculated from the bi-exponential decay profile, *i.e.*, $\tau_{avg} = (\alpha_1 \cdot \tau_1 + \alpha_2 \cdot \tau_2)/(\alpha_1 + \alpha_2)$, where α is the respective amplitude and τ is the decay component.[27] The τ_{avg} value diminished from 1.21 ns (**1**) to 0.95 ns (**1** + FA) upon FA interaction (Fig. 3d). Using the τ_{avg} value of the **1**-FA adduct and from the equation: $K_{SV} = Kq \cdot \tau$, the quenching rate constant (K_q) was calculated to be 9.37 × 10^{12} M^{-1} s^{-1}, suggesting a steady host–guest interaction.[75] Next, we construed the limit of detection (LOD) for the sensing event using the well-established equation: LOD = $3\sigma/k$, where σ is the standard deviation, estimated from the intensity values of five successive blank PL spectra of the sensor at a uniform time interval of ~1 min, and k is the slope derived from the PL intensity *vs.* [analyte] plot or its linear range.[59,80,81,89] Here, the σ value was evaluated as 12.4405 (Fig. S29 and Table S5, ESI†), while from the linear concentration range (0.014–0.03 × 1 mM) of intensity *vs.* concentration plot, the slope (k) was evaluated to be 4394.6605 (Fig. 30, ESI†). Therefore, the LOD was evaluated to be 8.49 μM (0.25 ppm). Such low LOD and high K_{SV} values obtained in the present study were found to be mostly superior (or comparable) with recently reported FA-sensors (Table S12, ESI†), which advocated the consistency of this probe. The quenching response was found to be fast. In a typical 'fast responsive

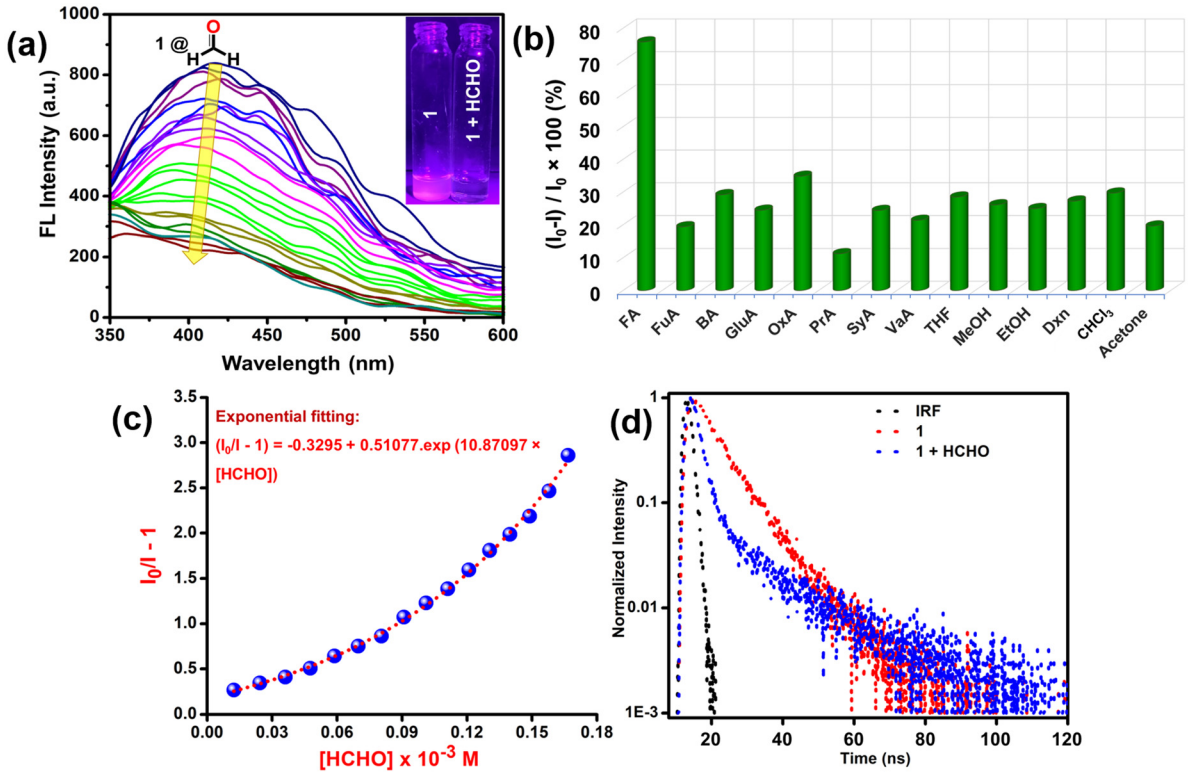

Fig. 3 (a) Fluorescence quenching of Mn-MOF (**1**) during gradual addition of 1 mM aqueous FA solution (inset: physical image of blue-emissive sensor and sensor @analyte adduct); (b) comparative bar diagram of the quenching efficiency for analytes; (c) stern–volmer ($I/I_0 - 1$ *vs.* concentration) plot, exhibiting a non-linear nature; and (d) lifetime decay profiles of **1** and **1** + FA as a result of dynamic quenching.

analyte' test, ~86% quenching of the MOF's emission happened in just 70 seconds when 400 μL of 1 mM FA solution was added at a time to the sensor dispersion (Fig. S31, ESI†). We also inspected the propensity of **1** towards FA under the influence of a competitive environment. We first added 200 μL of 1 mM competing analytes to the sensor emulsion placed inside the cuvette, and the PL intensity was recorded. Next, we added 200 μL of FA (1 mM) to these, and the intensity was noted. The same sequence of analyte addition was repeated one more time. This is schematically provided in Fig. 4a and b, which certified the exceptional specificity of **1** towards FA among the pool of aldehydes. Recyclability is a crucial factor for any sensor design. Here, the MOF-sensor exhibited almost unaltering quenching efficacy four times (75.47%, 74.53%, 76.05%, and 74.36% in cycles 1–4, standard deviation: ~0.80), which certainly escalates its on-field viability (Fig. S32, ESI†). In addition, the solid-state emissive behavior of **1** prompted us to explore the vapor phase sensing of FA since it is an indoor VOC with a high vapour pressure.[90] In this context, we adapted a previously studied set-up (see the Experimental section, ESI† and Fig. 4c, Fig. S33, ESI†), where the drop-cast MOF-film exhibited a broad shoulder at ~420 nm and a sharp peak at ~480 nm in its emission spectra (Fig. 4d). Upon exposure to FA vapor for 0–30 minutes, an excellent quenching (~57%) of the MOF's luminescence was apparent (Fig. 4d and e). The steep decrease in the fluorescence intensity was evidenced in the first 10–12 minutes for both 420 and 480 nm (Fig. S33, ESI†).

Based on the distinct spectroscopic outcome of the MOF-sensor (**1**) with the addition of different concentrations of interacting analyte FA, molecular logic gate operations were proposed. It is noteworthy that a logic gate is a kind of Boolean logic execution device that uses "1" to represent 'true value' or 'high signal' and "0" to represent "false value" or "low signal". The development of logic gates at the molecular level has drawn a lot of attention recently. Molecular logic gates are a subset of logic gates that carry out Boolean operations at the molecular level. It can perform logical operations based on one or more chemical inputs and respective signal outputs.[91,92] In this case, the specific spectroscopic responses of **1** in the presence of increasing concentrations of interacting analyte FA can further mimic an explicit progression of numerous logical functions, competent of performing molecular-level arithmetic computations. Here, we have designated the sensor (**1**) as input 1 (IN 1). Furthermore, the distinct FA concentrations (10, 15 and 25 ppm) have been assigned as input 2

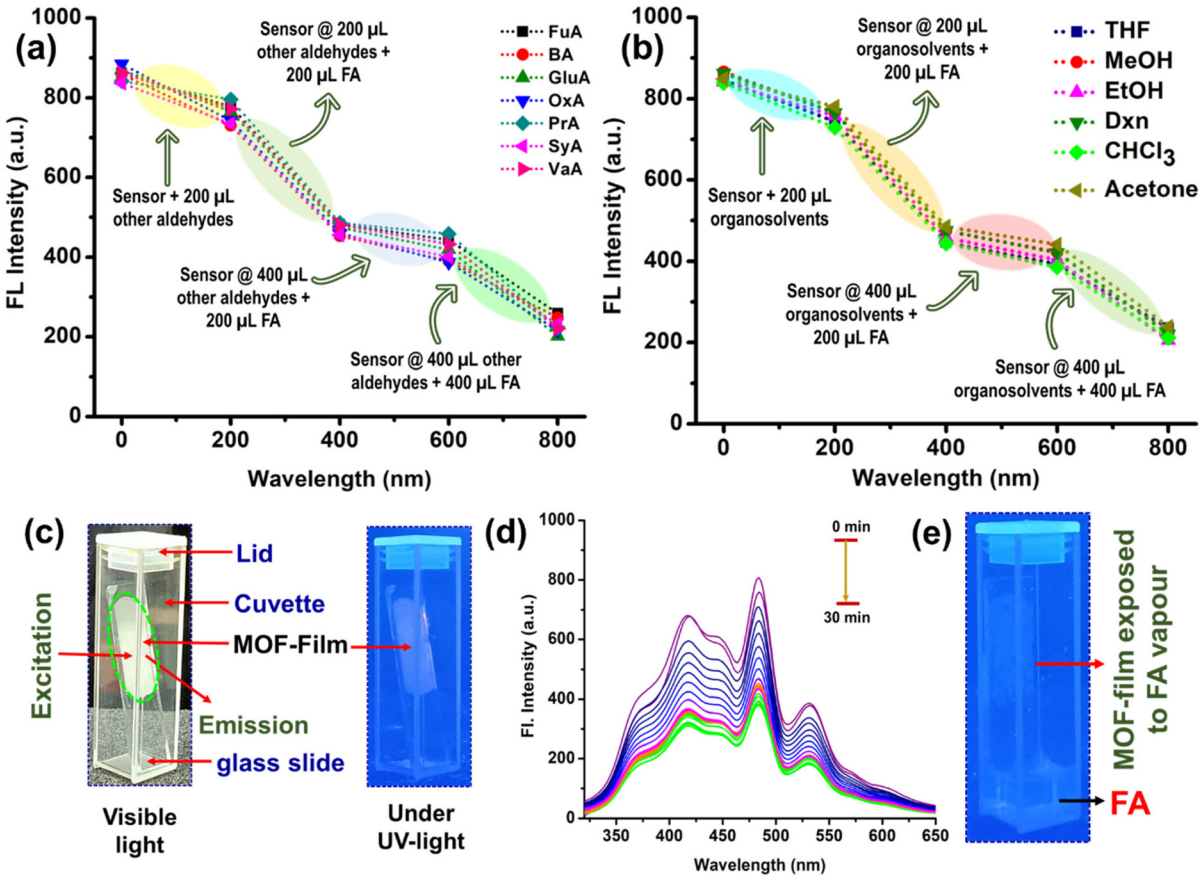

Fig. 4 (a and b) FA detection by **1** under a competitive environment: considering aldehydes (a) and organo-solvents (b), (c) physical image of the experimental set-up adapted for vapor phase FA sensing, (d) PL quenching (~57%) of **1** drop-cast on a quartz slide upon exposure to FA vapor for 0–30 minutes, and (e) quenched MOF-film under UV-light after exposure to FA vapor.

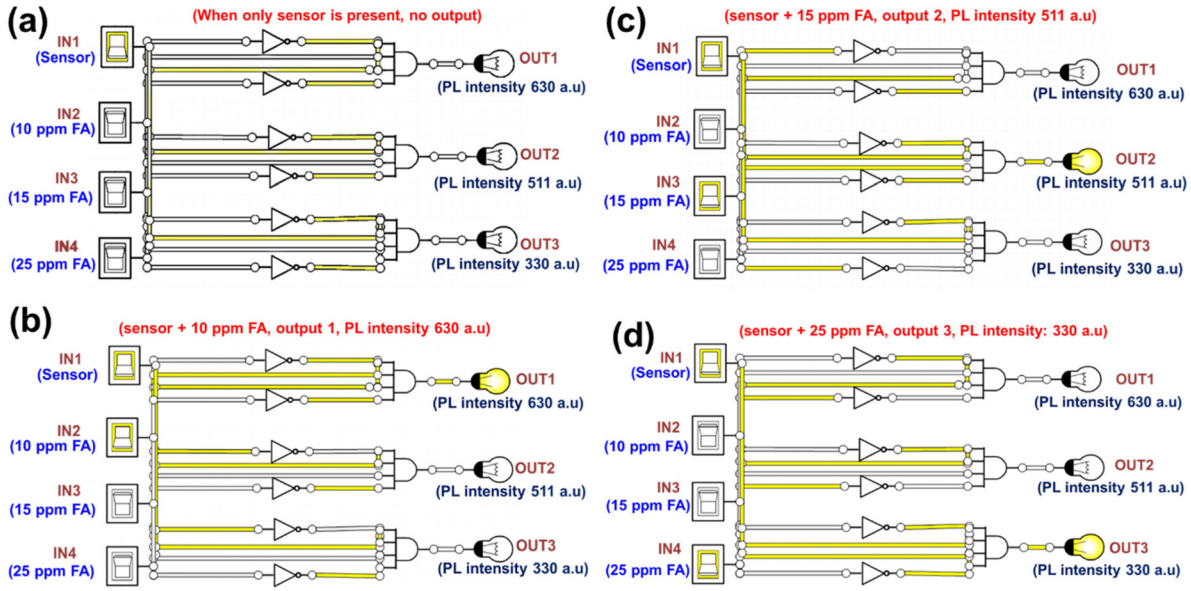

Fig. 5 Fabrication of logic gate with outputs (OUT1, OUT2, OUT3) upon varying inputs (AND-NOT logic functions) for sensor (**1**) with 10, 15 and 25 ppm of analyte (FA), where (a) IN1 : IN2 : IN3 : IN4 :: 1000, (b) IN1 : IN2 : IN3 : IN4 :: 1100, (c) IN1 : IN2 : IN3 : IN4 :: 1010, and (d) IN1 : IN2 : IN3 : IN4 :: 1001.

(IN 2), input 3 (IN 3) and input 4 (IN 4), respectively. We utilized 3 outputs here. The quenching signal, obtained after the addition of 10, 15, and 25 ppm of FA to the sensor dispersion (**1**), showing PL intensities of 630 a.u., 511 a.u. and 330 a.u. were appointed as the outputs (OUT1, OUT2 and OUT3) (Fig. 5 and Fig. S34, ESI†). The 4 inputs and 3 outputs were next used to formulate a unique logic circuitry, the corresponding truth table of which has been provided in Table S6, ESI.† Initially, the sensor (IN1) exhibits fluorescence intensity at 854 a.u. In this situation of IN1 = 1, there is no output signal. In the presence of 10 ppm FA (*i.e.*, IN2 = 1), the sensor exhibits reduced PL intensity (630 a.u.). This indicates that OUT1 will now be ON (*i.e.*, OUT1 = 1), while the other two outputs will be OFF. In the presence of 15 ppm FA (*i.e.*, IN2 = 1), the diminished PL intensity was found to be at 511 a.u. At this moment, OUT2 will be in an ON state (*i.e.*, OUT2 = 1), while OUT1 and OUT3 will be in an OFF state. Finally, in the presence of 25 ppm FA (IN3 = 1), the sensor unveiled PL intensity reduced to 330 a.u., demonstrating that now OUT3 will be ON (*i.e.*, OUT3 = 1), while keeping OUT1 and OUT2 OFF. Thus, the combined sequential AND-NOT logic gates can be utilized as molecular switches for the construction of memory devices in the future (Fig. 5).

Fluorescence 'turn-off' detection of Cr(VI) oxyanions

Recently, oxyanion/oxoanion sensing in several industrial effluents has become an urgent issue. This particular class of inorganic pollutants in oxoanionic forms presents greater environmental mobility and solubility in water streams (as compared to cationic forms).[93] In this pursuit, we extended our investigation of **1** towards oxoanion sensing. For this, we initially checked the fluorescence alteration of 1-acetonitrile sensor dispersion towards 10^{-4} M aqueous oxoanion (SO_4^{2-}, PO_4^{3-}, NO_3^-, MnO_4^-, ClO_4^-, OAc^-, CO_3^{2-}, AsO_4^{3-}, AsO_2^-, CrO_4^{2-}, and $Cr_2O_7^{2-}$) solutions (1 : 1 sensor : analyte v/v). From this, a noteworthy fluorescence quenching response was achieved in the case of Cr(VI) anions only, *i.e.*, chromate (CrO_4^{2-}) and dichromate ($Cr_2O_7^{2-}$), as presented in the inset of Fig. 6a and b. The PL titration was recorded during the incremental addition of 10^{-4} M aq. CrO_4^{2-} and $Cr_2O_7^{2-}$ solutions to MOF-dispersion (Fig. 6a and b, respectively). The initial emission profile of **1** and its concomitant reduction under the impact of the other oxoanion series are provided in Fig. S35, ESI.† The CIE plots of **1** before and after CrO_4^{2-} and $Cr_2O_7^{2-}$ sensing are shown in Fig. S36, ESI.† The decreasing order of quenching efficacy, as revealed by the oxoanions (Fig. 6d), was registered as $Cr_2O_7^{2-}$ (79.46%) > CrO_4^{2-} (76.37%) ≫ CO_3^{2-} (25.67%) > MnO_4^- (23.70%) > NO_3^- (22.54%) > SO_4^{2-} (20.41%) > AsO_2^- (17.22%) > OAc^- (16.54%) > AsO_4^{3-} (14.39%) > PO_4^{3-} (9.26%) > ClO_4^- (7.79%). The quenching plots were further interpreted by exploring the S–V plots. The $(I_0/I - 1)$ *vs.* [analyte] plots displayed an overall exponential fitting (*i.e.*, non-linear nature, *vide* Fig. 6c), indicating the possibility of resonance energy transfer (RET)[27,83] in the sensing event and concurrent occurrence of static and dynamic quenching.[27,94] From the linear range of the S–V plots (~0.002×10^{-4} to 0.022×10^{-4} M), the K_{SV} values were evaluated as 16.13×10^4 and 12.73×10^4 M^{-1} for CrO_4^{2-} and $Cr_2O_7^{2-}$, respectively (Fig. S37 and S38, ESI†). The influence of Cr(VI)-anions further altered the fluorescence lifetime value of **1**. The lifetime decay profiles depicted the τ_{avg} value to be 0.82 ns and 0.78 ns for **1**⋯CrO_4^{2-} and **1**⋯$Cr_2O_7^{2-}$ adducts (Fig. S39, ESI†). Using the

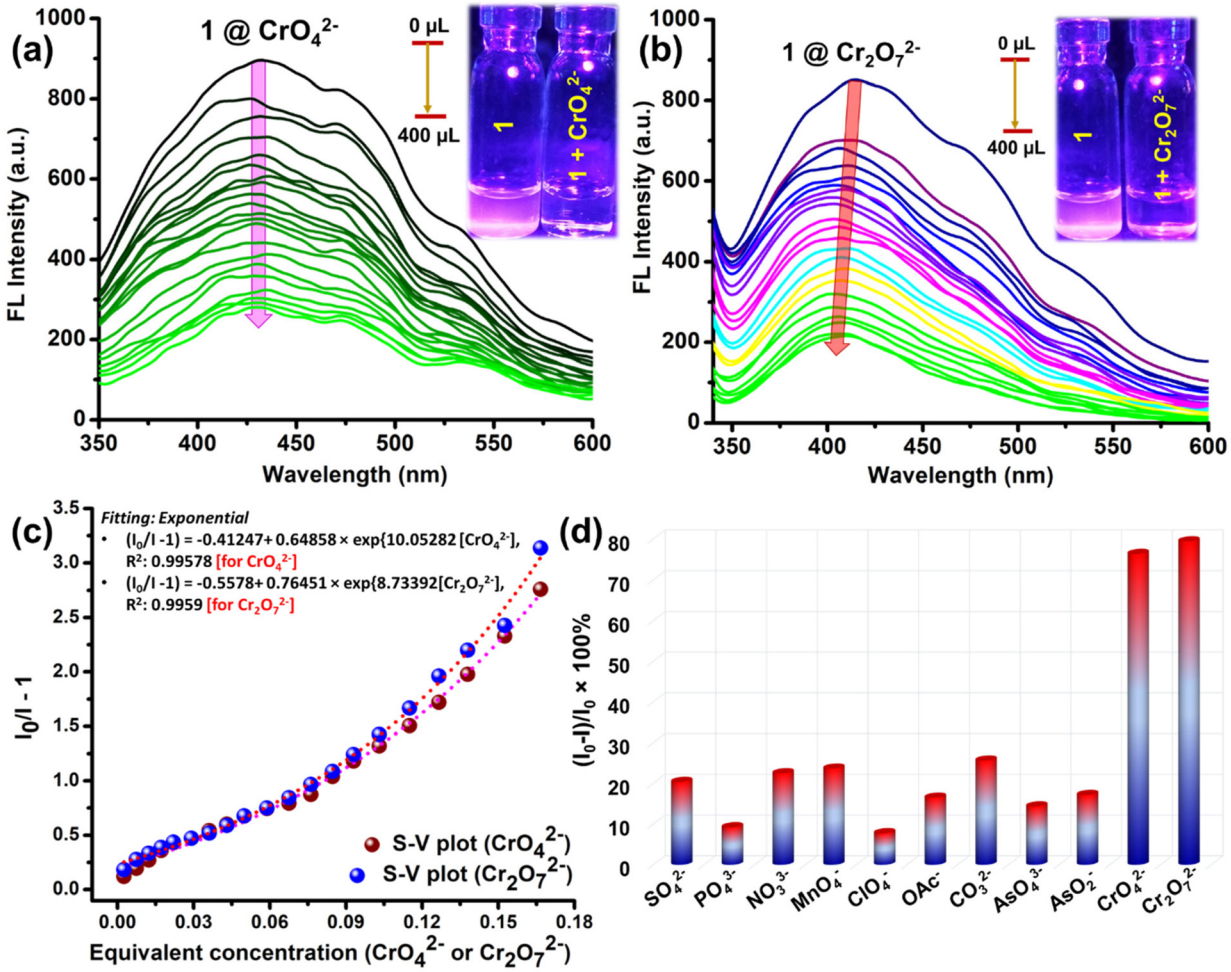

Fig. 6 Fluorescence quenching of **1** during gradual addition of aqueous 10^{-4} M (a) CrO_4^{2-} and (b) $Cr_2O_7^{2-}$ (inset: physical images of luminescence turn-off, sensor : analyte in 1 : 1 ratio); (c) Stern–Volmer plot and corresponding non-linear fitting for CrO_4^{2-} and $Cr_2O_7^{2-}$; and (d) comparison of the quenching efficiencies of the series of oxyanions.

τ_{avg} values, the quenching rate constants (K_q) were deduced as 19.67×10^{13} (for CrO_4^{2-}) and 16.32×10^{13} M^{-1} s^{-1} (for $Cr_2O_7^{2-}$). Next, the LODs were calculated using the $3\sigma/k$ equation. Accordingly, the same σ value was used as before (*i.e.*, 12.4405, Fig. S29, ESI†). The slope (K) was computed as 9030.262 and 6340.132 from the linear region of the intensity *vs.* equivalent [analyte] plot (Fig. S40 and S41, ESI†). Therefore, we obtained the LODs as 0.41 µM (79 ppb) and 0.59 µM (0.17 ppm) for CrO_4^{2-} and $Cr_2O_7^{2-}$.

Contemporary literature illustrates the present work to be substantially superior to lately studied sensors for the CrO_4^{2-} and $Cr_2O_7^{2-}$ in terms of analytical outcomes (LOD and K_{SV}), which certainly established the relevance of our work (Table S13, ESI†). The response time in Cr(VI)-sensing events was determined from the 'fast-responsive analyte' study performed in 0–400 s. Upon immediately adding the whole analyte solution, a significant degree of quenching (76.37% and 79.83%) was observed in just ~48 and ~40 s, for CrO_4^{2-} and $Cr_2O_7^{2-}$ (Fig. S42, ESI†). At this instance, the possibility of intervention in the sensing event from the other oxyanions (having the same formula of $A_xO_y^{z-}$, A is a chemical element except O) cannot be eliminated. In this context, the response of CrO_4^{2-} and $Cr_2O_7^{2-}$ towards **1** was examined in the presence of competing analytes. For this, first, the emission intensity of **1** was recorded, followed by the addition of 400 µL of 10^{-4} M oxoanion solutions to inspect the drop in PL intensity, and finally, 400 µL, 10^{-4} M CrO_4^{2-} and $Cr_2O_7^{2-}$ solutions were introduced in the **1**⋯ other oxyanion adduct. In both cases, unswerving quenching efficiency was recorded in the presence of a competing environment, as evidenced in Fig. S43 and S44, ESI.† Furthermore, we reviewed whether MOF's PL profile is regenerable or not! In the present work, the centrifuged, washed, and dried MOF exhibited rejuvenated inherent luminescence after the completion of one full sensing event, which was again employed for another cycle of sensing. The intact quenching efficacy (75.68 to 76.94% for CrO_4^{2-} and 78.03 to 79.36% for $Cr_2O_7^{2-}$) was sustained over six cycles, demonstrating six-fold recyclability for Cr(VI) sensing events (Fig. S45, ESI†).

Insight into the sensing mechanism

To analyze the underlying host–guest interaction for the FA and Cr(VI)-oxyanion sensing phenomenon, we performed density functional theory (DFT) calculations and several wet-chemical experimentations. In general, luminescent chemosensors are a fascinating area of study due to their versatile applications in detecting various analytes, from small ions to complex biomolecules. These sensors primarily function through several mechanisms, such as, (a) confinement of the analyte within the pores of the host, resulting positive interactions between the receptor and the analyte to produce a measurable change in luminescence; (b) a structural collapse or significant conformational change of the receptor under influence of the approaching analyte making it a valuable detection tool; (c) excited-state electron transfer, which can quench or enhance the luminescence of the host–guest, depending on the nature of the interaction; (d) resonance energy transfer (RET) including Förster resonance energy transfer (FRET) or dexter energy transfer; (e) interaction driven by weak electrostatic forces; (f) the inner-filter effect (IFE), involving absorption of excitation or emission light by the analyte without a direct link between the fluorescer and the absorber; (g) static quenching through the formation of a non-luminescent donor–acceptor complex at the ground state, thus preventing the emissive nature; (h) dynamic quenching, also known as collision-based quenching, involving collisions between the excited fluorophore and the quencher; (i) indicator displacement assay (IDA), where an indicator bound to the sensor is displaced by the analyte; (j) combination of mechanisms, often encompassing a fusion of two or more of the aforesaid mechanisms to achieve specific sensing capabilities and enhance sensitivity and selectivity.[27,59,79–81,88,95]

In this context, we first examined the powder XRD patterns of **1** before and after its involvement in the FA sensing event. For this, the **1**⋯ FA adduct was washed with water and dried overnight after one sensing cycle. We observed an almost intact PXRD pattern for **1** (Fig. S46, ESI†) before and after FA sensing. This ruled out the possibility of structural collapse or IDA.[27,75] The NLDFT half pore width of **1** after FA sensing was evaluated to be 14.05 Å from the N_2 adsorption–desorption study (Fig. S46b, ESI†). The negligible alteration in the pore width from that of bulk-synthesized **1** (14.48 Å) further ruled out the prospect of pore confinement. Consequently, we postulate that interface-driven interactions may be operating here. Firstly, it was observed that the UV-Vis spectrum of FA shows two absorption bands at ~225 nm (π–π*) and ~300 nm (n–π*),[96] while the excitation and emission band for the sensor was centered at 270 and 440 nm (spread over a region of ~270–700 nm here) respectively. Therefore, there is a possibility of spectral overlap between the absorption band of FA and that of the emission profile of the MOF within the edge of non-covalent radius distance.[50] Here, a slight spectral overlapping was evidenced between FA (excitation) and **1** (emission), advocating a very weak RET process (Fig. S47, ESI†). From the λ_{ex} and $\lambda_{emission}$ values, it is also clear that the prospect of competitive absorption of the incident light (of wavelength 270 nm) by FA while conducting the fluorescence titration is negligible, eliminating the aspect of IFE.[97] This is further supported by the UV-Vis absorption spectrum of the **1**⋯FA adduct, recorded during the incremental addition of 400 μL, 1 mM FA solution to the sensor dispersion (Fig. S48, ESI†), which didn't exhibit generation of any new absorption peak during the process. At this moment, an excited-state electron transfer pathway may be hypothesized to be responsible for the quenching mechanism. From literature, we realized that when the conduction band (CB) of the electron-affluent MOF is energetically higher than the lowest unoccupied molecular orbital (LUMO or π*) of the analyte, then the prospect of redistribution of excited-state electrons (of MOF) to the vacant orbitals of analyte always predominates.[50,59] To inspect this possibility, we performed DFT calculations of **1**, MOF-constituents, and the whole analyte series of aldehydes and organosolvents using Turbomole (V7.0) software (TmoleX interface 4.1.1),[98] using the B3LYP hybrid functional and def-SV(P) (C, N, O, H) and def2-TZVP (transition metal) basis sets. The HOMO and LUMO energy levels of phen, hia, and **1** and the electrostatic potential (ESP) surface is provided in Fig. S49 and S50, ESI.† For a practical PET pathway to occur, the LUMO of the analyte must be lower than the CB of the MOF (−0.92 eV here). It was observed that among the considered pool of analytes, the LUMOs of PrA (−0.52 eV), GluA (−0.66 eV), VaA (−0.55 eV), THF (1.68 eV), MeOH (1.82 eV), EtOH (1.71 eV), dioxane (1.73 eV), $CHCl_3$ (−0.37 eV) and acetone (−0.44 eV) were located above the CB of **1**, thus discarding the chance of effective PET (Table S7, ESI†). However, the analytes FA, SyA, OxA, BA, and FuA depicted their corresponding LUMOs to be situated at −1.03, −1.96, −2.88, −2.12, and −2.08 eV, which are lower than the CB of **1** (Table S7, ESI†). Therefore, it was perceived that the LUMO of FA was in closest proximity to that of the MOF's CB, owing to which the excited electrons of **1** jump to the analyte's LUMO and fail to return to the ground state during the relaxation process, causing the quenching phenomenon (shown schematically in Fig. 7). At this junction, we learn that quenching can be of two types: static or dynamic. The static mode of quenching manifests the host–guest complex formation in the ground state. So, appreciable amendment of the decay profiles (for sensor and sensor–analyte adduct) is not expected in static quenching.[76] In contrast, dynamic quenching, occurring from a collision between an excited fluorophore (receptor) and quencher, is undoubtedly an excited state phenomenon. Hence, a specific alteration in the fluorescence lifetime value (τ_{avg}) is expected here. Thus, the diminution in the τ_{avg} value from 1.21 ns (**1**) to 0.95 ns (**1** + FA) (Fig. 3d) recommended a spontaneous dynamic quenching in the FA sensing event.

Next, the sensing phenomenon towards CrO_4^{2-} and $Cr_2O_7^{2-}$ was explored. First, it was realized that the PXRD pattern of **1** before and after its participation in CrO_4^{2-} and $Cr_2O_7^{2-}$ sensing events were almost unaltered, thus eliminating the prospect of structural breakdown upon analyte interaction (Fig. S51a, ESI†). After one sensing cycle for CrO_4^{2-}

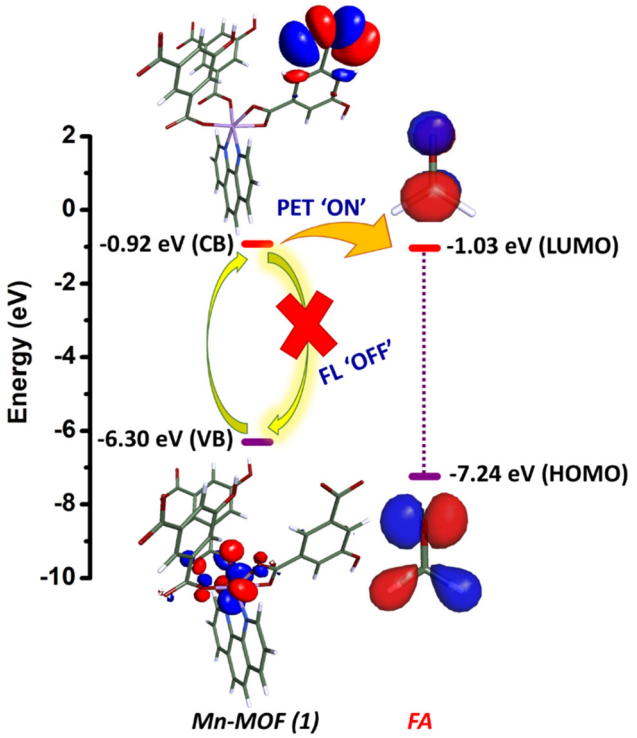

Fig. 7 Schematic illustration of the photo-induced electron transfer (PET) mechanism for FA sensing.

and $Cr_2O_7^{2-}$, the washed and dried MOF exhibited half pore width values (calculated by the NLDFT method, from the N_2 adsorption–desorption study at 77 K) of 14.76 and 13.86 Å (Fig. S51b, ESI†). This trivial variation of the pore parameters from the as-synthesized MOF (14.48 Å) possibly arose during the sample processing and, therefore excluded the likelihood of encapsulation of larger-sized Cr-oxyanions inside the pores of **1**. Therefore, the mechanistic pathway may be speculated as surface-based PET, or RET, or IFE, or electrostatic interactions, or any combination of two or more. At first, we calculated the HOMO and LUMO energy levels of the oxoanions and compared these with the MOF's CB to inspect the prospect of PET, which is quite less explored in the contemporary research domain of MOF sensors. The key findings in the PET mechanism depict that lower LUMO energy levels of analytes (here oxoanions) correlate with a better propensity to accept electrons from the MOF's CB, leading to greater QE% in PET processes. The chemical structure of the oxyanions used for DFT calculations are given in Fig. S52, ESI.† The HOMO and LUMO levels along with the orbital lobes of the oxoanions are provided in Table S8, ESI.† Given the LUMO energy levels of CrO_4^{2-} and $Cr_2O_7^{2-}$ are −6.82 eV and −6.98 eV, respectively, and the CB of the MOF is at −0.92 eV, the facile excited-state electron transfer from the CB of the MOF to the π* (LUMO) orbitals of the analytes is energetically favourable (Fig. 8b), supporting a strong PET mechanism in both cases. However, we observed that the LUMO of SO_4^{2-} (−8.44 eV), NO_3^- (−7.16 eV), CO_3^{2-} (−8.23 eV), and AsO_4^{3-} (−7.17 eV) lies further below the LUMOs of Cr(VI)-species, which may indicate a possibility of better PET to occur for these anions (Fig. S53, ESI†). Still, the quenching efficiencies of SO_4^{2-} (20.41%), NO_3^- (22.54%), CO_3^{2-} (25.67%), and AsO_4^{3-} (14.39%) were not as effective as those of CrO_4^{2-} and $Cr_2O_7^{2-}$. This suggests that PET is possibly not the sole governing mechanism in this context. To validate this hypothesis, we next examined the extent of spectral overlap between the absorption bands of the analytes and the emission band of the MOF, as shown in Fig. 8a. The UV-Vis absorption spectra of Cr(VI) anions span a range of approximately 225 to 480 nm, with peaks at around 270 nm and 370–380 nm. This range encompasses the entire excitation wavelength (270 nm) and the emission band (440 nm) of compound **1**. Consequently, a substantial spectral overlap occurs, resulting in resonance energy transfer (RET) between the receptor (**1**) and the quencher (Cr(VI)-oxoanions) and subsequent fluorescence quenching. Except for CrO_4^{2-} and $Cr_2O_7^{2-}$, four anions showed QEs > 20%, which are MnO_4^-, SO_4^{2-}, NO_3^-, and CO_3^{2-}. Among these four, only a fair amount of spectral overlap *i.e.*, RET was realized for MnO_4^-, which justifies its potency towards 23.70% quenching to the MOF's luminescence. This scenario also clarifies that PET was more dominant than RET for other anions like SO_4^{2-}, NO_3^-, CO_3^{2-}, AsO_4^{3-}, AsO_2^- and OAc^-, that explains the slight (~14–26%) fluorescence quenching for these species. At this time, the above facts also discarded the sole supremacy of one specific mechanism for Cr(VI)-oxoanion sensing and endorsed the synchronous existence of both RET and PET for the quenching phenomenon.

Now, the merging of the absorption bands of CrO_4^{2-} and $Cr_2O_7^{2-}$ with the emission band of **1** indicated the eventuality of the inner-filter effect (IFE). The IFE occurs when the analyte absorbs part of the excitation or emission light, leading to an apparent reduction in fluorescence intensity. To address this potential interference from IFE on the photoluminescence response of the fluorophore **1** in the presence of the quencher, the experimental PL data were corrected using a specific equation. The equation reads as, $I_{corr}/I_{obs} = 10^{[A(ex)+A(em)]/2}$, where I_{obs} and I_{corr} are the observed (during performing PL titration) and IFE-corrected PL intensity, I_{corr}/I_{obs} is called the correction factor, A(ex) and A(em) are the absorption values of the fluorophore (**1**) ····analyte (CrO_4^{2-}, $Cr_2O_7^{2-}$ adducts) adduct at excitation (270 nm) and emission (440 nm) wavelengths respectively.[88,95,97] In this context, we recorded the UV-Vis absorption spectrum for compound **1** while gradually adding 400 μL of 10^{-4} M CrO_4^{2-} and $Cr_2O_7^{2-}$ (Fig. S54 and S55, ESI†). The calculation of IFE parameters such as correction factor, I_{corr}, and QE_{corr} (%) at various concentrations of the analyte is provided in Tables S9 and S10, ESI.† The outcomes specified that the fluorescence suppression efficiency of the IFE for CrO_4^{2-} and $Cr_2O_7^{2-}$ reaches ~41.27 and ~26.40% (Fig. 8c, d and Fig. S56, S57, ESI†), indicating that IFE is one of the primary contributors to the PL quenching observed in this study. However, if the quenching was solely due to IFE, it would typically involve absorption of

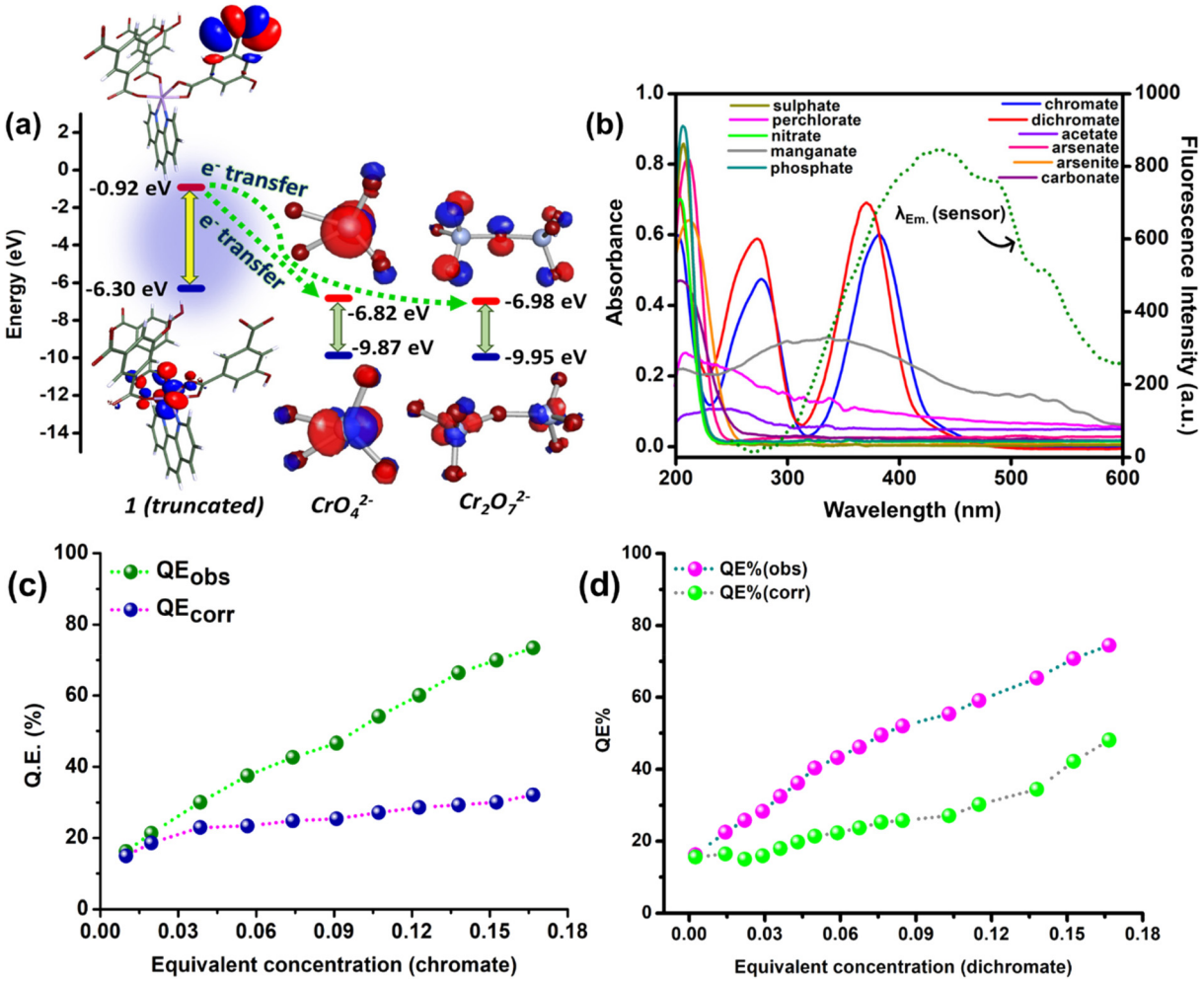

Fig. 8 (a) Photoinduced electron transfer (PET) from CB of **1** to the LUMO of analytes (CrO_4^{2-} and $Cr_2O_7^{2-}$), (b) resonance energy transfer (RET) between the absorption band of analytes with the emission profile of **1**, (c and d) comparison of observed and corrected quenching efficiency (QE, in %) for CrO_4^{2-} and $Cr_2O_7^{2-}$.

the excitation/emission light by the quencher entity before it reaches the fluorophore. So, the fluorescence lifetime of the fluorophore would generally remain unchanged, as the quencher primarily affects the intensity rather than the excited state lifetime. However, in the present study, we observed a reduction of the lifetime (τ_{avg}) values upon analyte interaction (0.82 and 0.78 ns for **1**$\cdots CrO_4^{2-}$ and **1**$\cdots Cr_2O_7^{2-}$ adducts from 1.21 ns in **1**), that established the coincident role of all three mechanistic pathways (IFE, RET, PET) in the quenching process. Additionally, due to their anionic nature, the targeted analytes will likely engage spontaneously in appreciable, electrostatic hydrogen bonding interactions. In this context, the surface-based host–guest interactions were further validated by the XPS study.[33,99,100] For this, powdered MOF (**1**) was soaked in 10^{-4} M aqueous CrO_4^{2-} and $Cr_2O_7^{2-}$ solutions for a few hours, filtered, oven-dried, and their XPS analysis was carried out. The high-resolution XPS survey spectra of CrO_4^{2-}/$Cr_2O_7^{2-}$ soaked samples exhibited the appearance of a weak Cr 2p peak (at ~578 eV) in both cases (Fig. S58 and S59, ESI†).[101] For **1**$\cdots CrO_4^{2-}$, the Mn 2p peak blue-shifted to a lower energy region (640.76 eV, from initial 641.12 eV for only MOF), while the O 1s and N 1s peak slightly shifted to higher energy regions (531.27 and 399.45 eV, from initial values of 531.072 and 399.07 eV) (Fig. S58, ESI†). Likewise, we observed that the N 1s and O 1s peaks shift to 399.26 eV and 531.40 eV from initial values of 399.037 and 531.09 eV after the interaction with $Cr_2O_7^{2-}$ (Fig. S59, ESI†). These observations, along with slight overall broadening or weakening of the Mn 2p, O 1s, and N 1s spectra, certainly confirmed the presence of weak electrostatic interactions between the MOF and the analytes due to differences in charge distribution.[27]

Therefore, taking all the above facts into consideration, it was convincingly concluded that the FA detection was predominantly guided by the PET pathway, while the multifaceted quenching response towards Cr(VI)-oxoanion species was governed by a unique combination of IFE-RET-PET and electrostatic interactions.

Detection of FA from fish, meat samples and wastewater specimens

Formaldehyde is commonly used to preserve raw food items (fish, meat, vegetables, *etc.*) to uphold the freshness component, particularly in the developing countries like India. FA may also be produced during the ageing or deterioration of raw flesh and other food samples. Therefore, the present study was extended for FA detection in fish and meat samples. We used *Labeo bata* (freshwater fish) and chicken as the fish and meat sources, and these were collected fresh from the local market in Durgapur (West Bengal, India). The samples were first cleaned with tap water and sliced into small pieces (<5 cm). Next, ~10 g of the food samples were ground in a mortar to prepare lumpy pastes and subsequently taken in a beaker to disperse in dil. HCl (100 ml, 100 mmol aq. solution) for breaking down the protein and collagens. At this moment, the samples were sonicated for the next 30 minutes, and a suitable volume of aqueous $NaHCO_3$ solution was added dropwise to adjust the pH to 6–7. The mixture was filtered using Whatmann 1 filter paper and the filtrate was used for further investigation (Fig. 9a). Using these extracts, 1 mM FA spiked samples were prepared. After 400 μL of FA-spiked fish and meat extracts were added to the sensor dispersion, noteworthy quenching of 72.14 and 70.64% was perceived (Fig. S60, ESI†). The observed QE% is excellent, considering the 75.82% quenching while taking FA in Milli-Q water (Fig. S61, ESI†). In addition, FA-spiked real-world water samples were prepared by taking sewage and tap water. The sewage water was collected from the in-house aqua rejuvenation plant in CMERI colony, Durgapur, and filtered before use. The tap water was collected from our wet-chemical lab. In both cases, we conducted a fluorescence titration study by steadily adding 400 μL, 1 mM FA-spiked samples to the sensor emulsion, and significant quenching was observed (72.53 and 70.45% for sewage and tap water, respectively) (Fig. S60 and S61, ESI†). In all four instances, 92–95% recovery of the quenching phenomenon was achieved w.r.to the control experiment. For deeper insights, the S–V plot ($I_0/I - 1$ *vs.* [HCHO]) was introduced in all four cases (Fig. 9b). The non-linearity of the S–V plots affirmed similar interactions in real-world samples in comparison to the Milli-Q water experiments (Fig. 9b). From the linear range of the S–V plots (Fig. S62, ESI†), the K_{SV} values were evaluated as 7.63×10^3 M^{-1}, 12.87×10^3 M^{-1}, 8.73×10^3 M^{-1} and 19.35×10^3 M^{-1} for fish, meat, sewage and tap water samples, which is comparable or even superior to the K_{SV} found during spectroscopic titration (8.90×10^3 M^{-1}) (Fig. 9c).

Detection of CrO_4^{2-} and $Cr_2O_7^{2-}$ from diverse wastewater samples

From the literature survey, the occurrence of heavy metal Cr (VI)-oxoanions in several industrial effluents was apparent. Therefore, considering this urgency of Cr(VI)-sensing from real-field specimens, we examined the sensing efficiency of **1** towards Cr(VI), solubilized in diverse, complex environmental matrices: coal mine wastewater (CMW), sewage water (SW), and tap water (TW). The preparation strategy of simulated 10^{-4} M Cr(VI)-oxoanion spiked solutions with CMW, SW, and TW is described in Table S11, ESI.† As presented in Fig. S63, ESI,† steady addition of 400 μL of 10^{-4} M $Cr_2O_7^{2-}$ and CrO_4^{2-} to the sensor dispersion depicted 76.85, 74.39 and 69% quenching

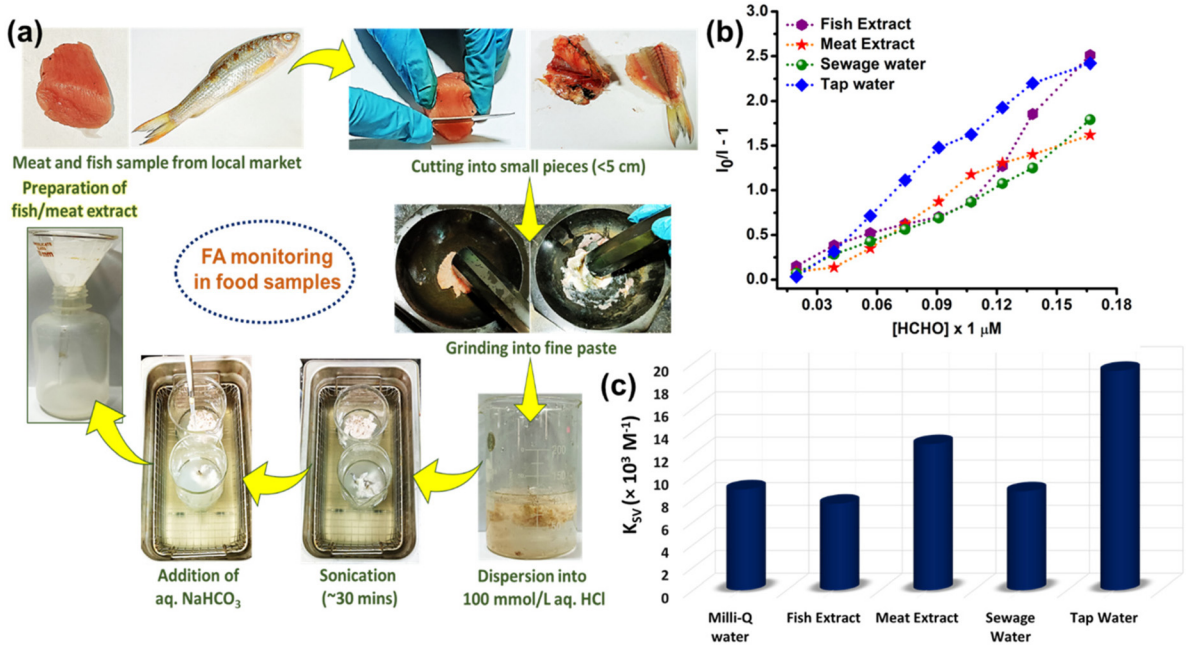

Fig. 9 FA detection from FA-spiked food samples and complex water specimens: (a) schematic representation of preparation of fish/meat extracts; (b) depiction of S–V plot for all considered specimens; and (c) bar diagram showing comparison of quenching constant (K_{SV}) found for lab-scale experiment (with Milli-Q water) and other food/wastewater samples.

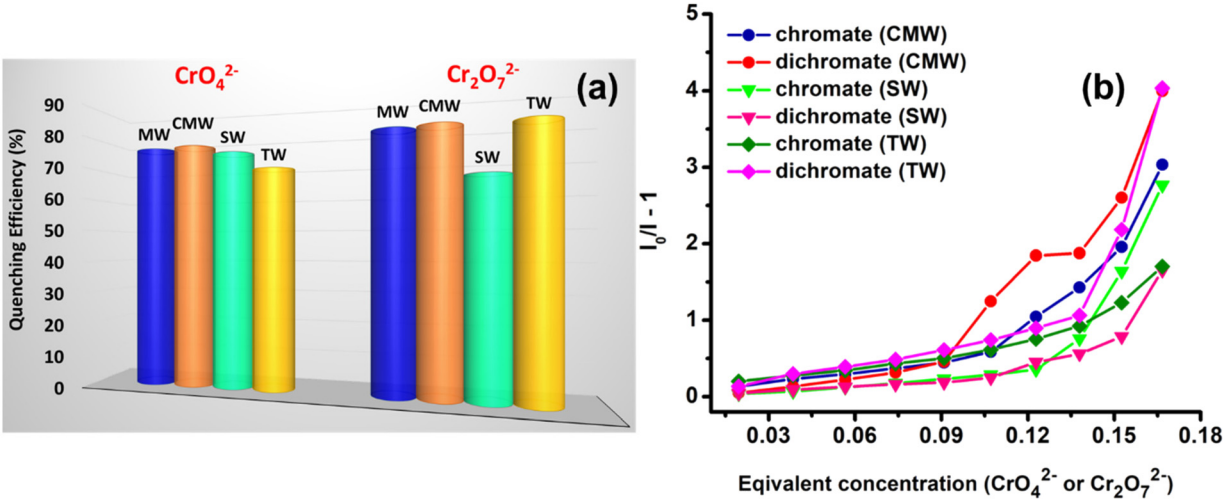

Fig. 10 (a) Depiction of comparative luminescence quenching efficiency (%) for CrO_4^{2-} and $Cr_2O_7^{2-}$ detection from Milli-Q water (MW) and other real water specimens *viz.* coal-mine wastewater (CMW), sewage water (SW), tap water (TW) and (b) corresponding non-liner Stern–Volmer plots.

(CME, SW and TW, respectively) for CrO_4^{2-} (recovery: ~90–101%) and 80.75, 65.52 and 80.12% quenching (CME, SW, and TW respectively) for $Cr_2O_7^{2-}$ (recovery: ~82–101%). The recorded results are satisfactory, considering the 76.37 and 79.46% quenching response for Cr(VI)-ions in Milli-Q water (Fig. 10a). Diving deep into the corresponding S–V plots exhibited non-linearity, thus implying dynamic quenching (Fig. 10b). The linear region of the S–V plot exhibited K_{SV} values of 4.89×10^4 (CMW), 3.10×10^4 (SW) and 5.17×10^4 (TW) M^{-1} for CrO_4^{2-}, while 5.62×10^4 (CMW), 2.16×10^4 (SW) and 7.03×10^4 (TW) M^{-1} for $Cr_2O_7^{2-}$ (see Fig. S64, ESI†). The obtained K_{SV} values are comparable to the values (16.13×10^4 and 12.73×10^4 M^{-1} for CrO_4^{2-} and $Cr_2O_7^{2-}$) from control titrations that confirmed the consistency of the probe.

Conclusion

In summary, this study reports the solvothermal synthesis and toxic analyte sensing properties of a water-stable Mn(II)-MOF presenting a 4-c net uninodal topology, a neutral secondary building unit (SBU) and linear 1D square channels forming a polymeric 2D network. The MOF (**1**) comprising a N-donor, highly fluorescent linker phen and a bridging co-ligand hia was explored for detecting biologically hazardous formaldehyde (FA) and high-valent oxoanion in the aqueous phase. The synthesized MOF (**1**) demonstrates phase purity, permanent mesoporosity, robust stability under harsh chemical conditions and high temperature, an irregular rod-like morphology, and uniform elemental distribution. In addition, Hirshfeld surface analysis and NCI-RDG plot confirmed the presence of π–π stacking and weak interactions in **1**. Its bright blue emission and photostability enable highly specific, ultrasensitive, and fast-responsive (~70 s) fluorescence turn-off detection of FA, achieving excellent analytical outcomes (LOD: 0.25 ppm, K_{SV}: 8.90×10^3 M^{-1}, K_q: 9.37×10^{12} M^{-1} s^{-1}). Moreover, vapour phase chemosensing of FA resulted in ~57% quenching rate. Based on the stimulating spectroscopic data in FA detection, a 04-input-03-output molecular logic gate was also proposed, which can be helpful in preparing molecular switches in the future. Furthermore, **1** serves as an efficient, ppb-level, recyclable probe (up to 06 times) for turn-off monitoring of Group-I carcinogenic CrO_4^{2-} and $Cr_2O_7^{2-}$ ions, with very low LODs (79 and 170 ppb), high K_{SV} values (16.13×10^4 and 12.73×10^4 M^{-1}), and rapid response times (~48 and ~40 s). Mechanistic insights derived from DFT calculations along with specific experimental investigations revealed that the FA detection process involves an excited-state electron transfer pathway (PET), while united contributions from IFE, PET, RET, collisional quenching, and weak hydrogen-bonding explained the Cr(VI)-sensing mechanism. Additionally, successful quantification of FA and Cr-oxoanions was achieved from various complex environmental matrices (*viz.*, raw fish and meat samples, sewage and wastewater) with excellent recovery rates (~92–95% for FA, ~90–101% for CrO_4^{2-}, and ~82–101% for $Cr_2O_7^{2-}$). These superior results highlight the potential of versatile porous materials for addressing emerging environmental challenges.

Author contributions

Udayan Mondal: conceptualization, data curation, formal analysis, investigation, methodology, software, and writing – original draft; Somrita Nag: data curation, formal analysis, and software; Rajeshwari Pal: data curation, formal analysis, and software; Priyabrata Banerjee: conceptualization, data curation, formal analysis, investigation, methodology, software, project administration, supervision, and writing – review & editing.

Data availability

The data supporting the findings of this study are available within the article and its ESI.†

Conflicts of interest

There are no conflicts to declare.

Acknowledgements

U.M. is grateful to the CSIR-HRDG for the SRF-Direct fellowship (Award Letter No. 31/0019(18584)/2024-EMR-I). U.M. is thankful to the Central Instrumentation Division, CSIR-IICB, Kolkata for extending the SCXRD facility. U.M. sincerely thanks Ms. Kumari Raksha, Research Scholar, IISER Kolkata for many insightful discussions. P.B. acknowledges the DST SERB-CRG sponsored project, GAP-240712 (*vide* reference no. CRG/2022/001679) for assistance.

References

1 D. Briggs, *Br. Med. Bull.*, 2003, **68**, 1–24.
2 P. Ghorai, U. Mondal, A. Hazra and P. Banerjee, *Coord. Chem. Rev.*, 2024, **518**, 216085.
3 U. Mondal, S. Nag, A. K. Batabyal, H. Hirani and P. Banerjee, *J. Environ. Chem. Eng.*, 2021, **9**, 105518.
4 Y. Zhang and B. Yan, *J. Mater. Chem. C*, 2019, **7**, 5652–5657.
5 Z. Tong, C. Han, W. Luo, X. Wang, H. Li, H. Luo, J. Zhou, J. Qi and R. He, *Age*, 2013, **35**, 583–596.
6 S. K. Patra, A. Patra, F. Rizzi, T. C. Ghosh and S. Bettuzzi, *Cancer Metastasis Rev.*, 2008, **27**, 315–334.
7 G. Jia, Y. Fu, X. Zhao, Q. Dai, G. Zheng, Y. Yang, C. Yi, T. Lindahl, T. Pan, Y.-G. Yang and C. He, *Nat. Chem. Biol.*, 2011, **7**, 885–887.
8 R. M. Kohli and Y. Zhang, *Nature*, 2013, **502**, 472–479.
9 S. Nandi, E. Sharma, V. Trivedi and S. Biswas, *Inorg. Chem.*, 2018, **57**, 15149–15157.
10 Z. Zhao, J. Hao, X. Song, S. Ren and C. Hao, *RSC Adv.*, 2015, **5**, 49752–49758.
11 S. Bej, S. Mandal, A. Mondal, T. K. Pal and P. Banerjee, *ACS Appl. Mater. Interfaces*, 2021, **13**, 25153–25163.
12 L. Feng, C. J. Musto and K. S. Suslick, *J. Am. Chem. Soc.*, 2010, **132**, 4046–4047.
13 E.-X. Chen, H. Yang and J. Zhang, *Inorg. Chem.*, 2014, **53**, 5411–5413.
14 A. Hempel-Jørgensen, S. K. Kjærgaard, L. Mølhave and K. H. Hudnell, *Arch. Environ. Health*, 1999, **54**, 416–424.
15 H. Che, Y. Li, X. Tian, C. Yang, L. Lu and Y. Nie, *J. Hazard. Mater.*, 2021, **410**, 124624.
16 Y.-B. Wei, M.-J. Wang, D. Luo, Y.-L. Huang, M. Xie, W. Lu, X. Shu and D. Li, *Mater. Chem. Front.*, 2021, **5**, 2416–2424.
17 Z. He, Y. Zhang and W. Wei, *Build. Environ.*, 2012, **47**, 197–204.
18 K. Kawamura, K. Kerman, M. Fujihara, N. Nagatani, T. Hashiba and E. Tamiya, *Sens. Actuators, B*, 2005, **105**, 495–501.
19 California Department of Public Health, *Formaldehyde*, 2011.
20 New Jersey Department of Health, *Hazardous Substance Fact Sheet*, 2016.
21 B. Parmar, Y. Rachuri, K. K. Bisht, R. Laiya and E. Suresh, *Inorg. Chem.*, 2017, **56**, 2627–2638.
22 Z.-J. Li, H.-D. Xue, Y.-X. Ma, Q. Zhang, Y.-C. Li, M. Xie, H.-L. Qi and X.-D. Zheng, *ACS Appl. Mater. Interfaces*, 2019, **11**, 46197–46204.
23 S. Nag, U. Mondal, H. Hirani, D. Chakraborty, A. Bhaumik and P. Banerjee, *Environ. Sci. Pollut. Res.*, 2022, **29**, 77821–77838.
24 U. Mondal, S. Nag and P. Banerjee, *Reference Module in Materials Science and Materials Engineering*, Elsevier, 2023.
25 D. Dey, S. Nag, U. Mondal, G. Majumdar and P. Banerjee, *Reference Module in Materials Science and Materials Engineering*, Elsevier, 2023.
26 K. Wu, J. Zheng, Y.-L. Huang, D. Luo, Y. Y. Li, W. Lu and D. Li, *J. Mater. Chem. C*, 2020, **8**, 16974–16983.
27 U. Mondal, K. Raksha, P. Mondal and P. Banerjee, *Chem. – Asian J.*, 2024, e202400374.
28 C. Gogoi and S. Biswas, *Cryst. Growth Des.*, 2021, **21**, 2680–2689.
29 X. Lai, D. Sun, Y. Hou, Y. Zuo, Y. Li and L. Zhang, *Adv. Mater. Interfaces*, 2018, **5**, 1800630.
30 T. He, Y.-Z. Zhang, X.-J. Kong, J. Yu, X.-L. Lv, Y. Wu, Z.-J. Guo and J.-R. Li, *ACS Appl. Mater. Interfaces*, 2018, **10**, 16650–16659.
31 P.-K. Lee, S. Yu, H. J. Chang, H. Y. Cho, M.-J. Kang and B.-G. Chae, *Sci. Rep.*, 2016, **6**, 36088.
32 A. Zhitkovich, *Chem. Res. Toxicol.*, 2005, **18**, 3–11.
33 K. Ma, J. Li, H. Ma, Y. Yang, H. Yang, J. Lu, Y. Li, J. Dou, S. Wang and S. Liu, *Chin. Chem. Lett.*, 2023, **34**, 108227.
34 S. Li, L. Lu, M. Zhu, C. Yuan and S. Feng, *Sens. Actuators, B*, 2018, **258**, 970–980.
35 Z.-J. Lin, H.-Q. Zheng, H.-Y. Zheng, L.-P. Lin, Q. Xin and R. Cao, *Inorg. Chem.*, 2017, **56**, 14178–14188.
36 M.-N. Georgaki, M. Charalambous, N. Kazakis, M. A. Talias, C. Georgakis, T. Papamitsou and C. Mytiglaki, *Environments*, 2023, **10**, 33.
37 Y. Liu, Z. Chen, W. Li, C. Ma, P. Wu, X. Wu, S. Li and S. Liu, *Microchim. Acta*, 2018, **185**, 470.
38 B. Wen, *Talanta*, 2002, **56**, 681–687.
39 M. Derbyshire, A. Lamberty and P. H. E. Gardiner, *Anal. Chem.*, 1999, **71**, 4203–4207.
40 V. Raveendran and R. N. Kizhakayil, *ACS Omega*, 2021, **6**, 23475–23484.
41 S. Pan, S. Roy, N. Choudhury, P. P. Behera, K. Sivaprakasam, L. Ramakrishnan and P. De, *Sci. Technol. Adv. Mater.*, 2022, **23**, 49–63.

42 Y. Zhang, Y. Liu, F. Huo, B. Zhang, W. Su and X. Yang, *ACS Appl. Nano Mater.*, 2022, **5**, 9223–9229.
43 C.-S. Cao, H.-C. Hu, H. Xu, W.-Z. Qiao and B. Zhao, *CrystEngComm*, 2016, **18**, 4445–4451.
44 B. B. Rath and J. J. Vittal, *Inorg. Chem.*, 2020, **59**, 8818–8826.
45 J.-P. Dong, B. Li, Y.-J. Jin and L.-Y. Wang, *CrystEngComm*, 2021, **23**, 1677–1683.
46 J. Xu, Y. Xu and X. Bu, *Small*, 2021, **17**, 2102331.
47 C.-A. Wang, K. Nie, G.-D. Song, Y.-W. Li and Y.-F. Han, *RSC Adv.*, 2019, **9**, 8239–8245.
48 M. Kariem, M. Yawer and H. N. Sheikh, *J. Solid State Chem.*, 2015, **231**, 239–247.
49 A. Hazra, S. Bej, A. Mondal, N. C. Murmu and P. Banerjee, *ACS Omega*, 2020, **5**, 15949–15961.
50 D. Chakraborty, S. Bej, S. Sahoo, S. Chongdar, A. Ghosh, P. Banerjee and A. Bhaumik, *ACS Sustainable Chem. Eng.*, 2021, **9**, 14224–14237.
51 J.-L. Ni, J.-J. Shao, Y. Liang, G.-J. Li, J.-F. Li, A. Mensah, L.-Z. Chen and F.-M. Wang, *J. Mol. Struct.*, 2022, **1257**, 132485.
52 F. Wang, C. Wang, Z. Yu, K. Xu, X. Li and Y. Fu, *Polyhedron*, 2016, **105**, 49–55.
53 S. L. Tan, M. M. Jotani and E. R. T. Tiekink, *Acta Crystallogr., Sect. E: Crystallogr. Commun.*, 2019, **75**, 308–318.
54 P. R. Spackman, M. J. Turner, J. J. McKinnon, S. K. Wolff, D. J. Grimwood, D. Jayatilaka and M. A. Spackman, *J. Appl. Crystallogr.*, 2021, **54**, 1006–1011.
55 N. C. Jana, P. Ghorai, P. Brandão, P. Bandyopadhyay, A. Saha, A. Frontera and A. Panja, *Inorg. Chim. Acta*, 2022, **531**, 120702.
56 S. Mandal, S. Bej and P. Banerjee, *J. Mol. Liq.*, 2023, **381**, 121789.
57 S. Mandal, D. Dey and P. Banerjee, *Tribol. Int.*, 2024, **195**, 109567.
58 M. Aetizaz, F. Ullah, S. Sarfaraz, T. Mahmood and K. Ayub, *RSC Adv.*, 2023, **13**, 29231–29241.
59 S. Chongdar, U. Mondal, T. Chakraborty, P. Banerjee and A. Bhaumik, *ACS Appl. Mater. Interfaces*, 2023, **15**, 14575–14586.
60 S. Malik, U. Mondal, N. C. Jana, P. Banerjee and A. Saha, *Dalton Trans.*, 2024, **53**, 12995–13011.
61 Y. M. Dai, S. C. Tang, J. Q. Peng, H. Y. Chen, Z. X. Ba, Y. J. Ma and X. K. Meng, *Mater. Lett.*, 2014, **130**, 107–110.
62 Y. Khan, S. K. Durrani, M. Mehmood and M. R. Khan, *J. Mater. Res.*, 2011, **26**, 2268–2275.
63 M. Sun, B. Lan, T. Lin, G. Cheng, F. Ye, L. Yu, X. Cheng and X. Zheng, *CrystEngComm*, 2013, **15**, 7010.
64 H. He, Q. Sun, W. Gao, J. A. Perman, F. Sun, G. Zhu, B. Aguila, K. Forrest, B. Space and S. Ma, *Angew. Chem., Int. Ed.*, 2018, **57**, 4657–4662.
65 J. Łuczak, M. Kroczewska, M. Baluk, J. Sowik, P. Mazierski and A. Zaleska-Medynska, *Adv. Colloid Interface Sci.*, 2023, **314**, 102864.
66 A. Shchukarev and D. Korolkov, *Open Chem.*, 2004, **2**, 347–362.
67 B. J. Matsoso, K. Ranganathan, B. K. Mutuma, T. Lerotholi, G. Jones and N. J. Coville, *New J. Chem.*, 2017, **41**, 9497–9504.
68 Z. J. Tang, P. Fang, J. H. Huang and P. Y. Zhong, *IOP Conf. Ser. Earth Environ. Sci.*, 2017, **100**, 012207.
69 G. P. López, D. G. Castner and B. D. Ratner, *Surf. Interface Anal.*, 1991, **17**, 267–272.
70 J.-C. Chou, Y.-L. Chen, M.-H. Yang, Y.-Z. Chen, C.-C. Lai, H.-T. Chiu, C.-Y. Lee, Y.-L. Chueh and J.-Y. Gan, *J. Mater. Chem. A*, 2013, **1**, 8753.
71 H. W. Nesbitt and D. Banerjee, *Am. Mineral.*, 1998, **83**, 305–315.
72 K. Natarajan, M. Saraf and S. M. Mobin, *Nanoscale*, 2018, **10**, 13250–13260.
73 H. Peng, Z. Mo, S. Liao, H. Liang, L. Yang, F. Luo, H. Song, Y. Zhong and B. Zhang, *Sci. Rep.*, 2013, **3**, 1765.
74 M. Thommes, K. Kaneko, A. V. Neimark, J. P. Olivier, F. Rodriguez-Reinoso, J. Rouquerol and K. S. W. Sing, *Pure Appl. Chem.*, 2015, **87**, 1051–1069.
75 P. Das and S. K. Mandal, *ACS Appl. Mater. Interfaces*, 2018, **10**, 25360–25371.
76 S. Bhattacharjee, S. Bera, R. Das, D. Chakraborty, A. Basu, P. Banerjee, S. Ghosh and A. Bhaumik, *ACS Appl. Mater. Interfaces*, 2022, **14**, 20907–20918.
77 C. Schlumberger and M. Thommes, *Adv. Mater. Interfaces*, 2021, **8**, 2002181.
78 S. S. Singh, *Z. Naturforsch. A*, 1969, **24**, 2015–2016.
79 R. Goswami, N. Seal, S. R. Dash, A. Tyagi and S. Neogi, *ACS Appl. Mater. Interfaces*, 2019, **11**, 40134–40150.
80 P. Ghorai, A. Hazra, J. Mandal, S. Malik, P. Brandão, P. Banerjee and A. Saha, *Inorg. Chem.*, 2023, **62**, 98–113.
81 U. Mondal, S. Bej, A. Hazra, S. Mandal, T. K. Pal and P. Banerjee, *Dalton Trans.*, 2022, **51**, 2083–2093.
82 B. Dutta, A. Hazra, A. Dey, C. Sinha, P. P. Ray, P. Banerjee and M. H. Mir, *Cryst. Growth Des.*, 2020, **20**, 765–776.
83 P. Ghorai, A. Dey, A. Hazra, B. Dutta, P. Brandão, P. P. Ray, P. Banerjee and A. Saha, *Cryst. Growth Des.*, 2019, **19**, 6431–6447.
84 Y. Zhang, S. Yuan, G. Day, X. Wang, X. Yang and H.-C. Zhou, *Coord. Chem. Rev.*, 2018, **354**, 28–45.
85 Y. Cui, Y. Yue, G. Qian and B. Chen, *Chem. Rev.*, 2012, **112**, 1126–1162.
86 G. Yang, X. Jiang, H. Xu and B. Zhao, *Small*, 2021, **17**, 2005327.
87 J. Maillard, K. Klehs, C. Rumble, E. Vauthey, M. Heilemann and A. Fürstenberg, *Chem. Sci.*, 2021, **12**, 1352–1362.
88 A. S. Tanwar, S. Patidar, S. Ahirwar, S. Dehingia and P. K. Iyer, *Analyst*, 2019, **144**, 669–676.
89 B. Dutta, A. Hazra, S. Datta, C. Sinha, P. Banerjee and M. H. Mir, *ACS Appl. Polym. Mater.*, 2022, **4**, 2841–2850.
90 R. Spence and W. Wild, *J. Chem. Soc.*, 1935, 506.
91 L. Liu, P. Liu, L. Ga and J. Ai, *ACS Omega*, 2021, **6**, 30189–30204.

92 J. Liu, T. Zhang, X. Liu, J. W. Y. Lam, B. Z. Tang and Y. Chau, *Mater. Horiz.*, 2022, **9**, 2443–2449.
93 A. D. Pournara, D. A. Evangelou, C. Roukounaki, E. K. Andreou, G. S. Armatas, T. Lazarides and M. J. Manos, *Dalton Trans.*, 2022, **51**, 17301–17309.
94 S. Khan, A. Hazra, B. Dutta, Akhtaruzzaman, M. J. Raihan, P. Banerjee and M. H. Mir, *Cryst. Growth Des.*, 2021, **21**, 3344–3354.
95 A. S. Tanwar, S. Hussain, A. H. Malik, M. A. Afroz and P. K. Iyer, *ACS Sens.*, 2016, **1**, 1070–1077.
96 M. R. Leonardo, L. A. B. da Silva, M. T. Filho and R. S. da Silva, *Oral Surg. Oral Med. Oral Pathol. Oral Radiol. Endod.*, 1999, **88**, 221–225.
97 S. Chen, Y.-L. Yu and J.-H. Wang, *Anal. Chim. Acta*, 2018, **999**, 13–26.
98 C. Steffen, K. Thomas, U. Huniar, A. Hellweg, O. Rubner and A. Schroer, *J. Comput. Chem.*, 2010, **31**, 2967–2970.
99 Y.-W. Li, J. Li, X.-Y. Wan, D.-F. Sheng, H. Yan, S.-S. Zhang, H.-Y. Ma, S.-N. Wang, D.-C. Li, Z.-Y. Gao, J.-M. Dou and D. Sun, *Inorg. Chem.*, 2021, **60**, 671–681.
100 J. Li, K.-X. Ma, Y. Yang, H. Yang, J. Lu, D.-C. Li, J.-M. Dou, H.-Y. Ma, S.-N. Wang and Y.-W. Li, *J. Mater. Chem. C*, 2022, **10**, 8979–8993.
101 Y. Chen, D. An, S. Sun, J. Gao and L. Qian, *Materials*, 2018, **11**, 269.